Received: 17 February 2024 | Revised: 16 March 2024 | Accepted: 2 April 2024

DOI: 10.1002/jat.4613

RESEARCH ARTICLE

Journal of Applied Toxicology WILEY

Cytotoxicity and toxicoproteomics analysis of thiazolidinedione exposure in human-derived cardiomyocytes

Abdullah Al Sultan [1,2] | Zahra Rattray [1] | Nicholas J. W. Rattray [1]

[1]Strathclyde Institute of Pharmacy and Biomedical Sciences, University of Strathclyde, Glasgow, UK

[2]Faculty of Pharmacy, Kuwait University, Safat, Kuwait

Correspondence
Nicholas J. W. Rattray, Strathclyde Institute of Pharmacy and Biomedical Sciences, University of Strathclyde, 161 Cathedral Street, Glasgow G4 0RE, UK.
Email: nicholas.rattray@strath.ac.uk

Abstract

Thiazolidinediones (TZDs) (e.g. pioglitazone and rosiglitazone), known insulin sensitiser agents for type II diabetes mellitus, exhibit controversial effects on cardiac tissue. Despite consensus on their association with increased heart failure risk, limiting TZD use in diabetes management, the underlying mechanisms remain uncharacterised. Herein, we report a comprehensive in vitro investigation utilising a novel toxicoproteomics pipeline coupled with cytotoxicity assays in human adult cardiomyocytes to elucidate mechanistic insights into TZD cardiotoxicity. The cytotoxicity assay findings showed a significant loss of mitochondrial adenosine triphosphate production upon exposure to either TZD agents, which may underpin TZD cardiotoxicity. Our toxicoproteomics analysis revealed that mitochondrial dysfunction primarily stems from oxidative phosphorylation impairment, with distinct signalling mechanisms observed for both agents. The type of cell death differed strikingly between the two agents, with rosiglitazone exhibiting features of caspase-dependent apoptosis and pioglitazone implicating mitochondrial-mediated necroptosis, as evidenced by the protein upregulation in the phosphoglycerate mutase family 5–dynamin-related protein 1 axis. Furthermore, our analysis revealed additional mechanistic aspects of cardiotoxicity, showcasing drug specificity. The downregulation of various proteins involved in protein machinery and protein processing in the endoplasmic reticulum was observed in rosiglitazone-treated cells, implicating proteostasis in the rosiglitazone cardiotoxicity. Regarding pioglitazone, the findings suggested the potential activation of the interplay between the complement and coagulation systems and the disruption of the cytoskeletal architecture, which was primarily mediated through the integrin-signalling pathways responsible for pioglitazone-induced myocardial contractile failure. Collectively, this study unlocks substantial mechanistic insight into TZD cardiotoxicity, providing the rationale for future optimisation of antidiabetic therapies.

KEYWORDS

label-free protein quantification, mitochondrial dysfunction, thiazolidinediones, WGCNA

1 | INTRODUCTION

Thiazolidinediones (TZDs, or glitazones), a class of insulin-sensitising agents, encompass a pair of agents, pioglitazone (PGZ) and rosiglitazone (ROSI), which are currently available for managing insulin resistance in patients with type 2 diabetes mellitus (T2DM) (Association, 2023). TZDs are potent and selective ligands of the nuclear peroxisome proliferator-activated receptor gamma (PPAR-γ), the molecular target responsible for insulin-enhancing effects (Wajid et al., 2019). Moreover, numerous ex vivo and in vivo studies have found that ligand activation of PPAR-γ regulates endothelial nitric oxide synthase, the enzyme primarily responsible for vascular nitric oxide production (Tan et al., 2021). Collectively, these promising data suggest that TZDs may exert cardioprotective effects in addition to their well-recognised hypoglycaemic effects. However, the cardiovascular effects of TZDs reported in clinical trials, pharmacovigilance reports and animal models have been surprisingly inconsistent and controversial. Table 1 provides an overview of key findings from meta-analyses of the TZDs used and their associated cardiovascular effects (de Jong et al., 2017; Lago et al., 2007; Liao et al., 2017; Nissen & Wolski, 2007, 2010; Richter et al., 2007; S. Singh et al., 2007a, 2007b; Wallach et al., 2020; Zhou et al., 2020).

While the meta-analyses' findings (Table 1) revealed distinct cardiac profiles for PGZ and ROSI, a concerning consensus emerged regarding their shared association with an increased risk of heart failure (HF) (de Jong et al., 2017; Lago et al., 2007; Liao et al., 2017; Nissen & Wolski, 2007, 2010; Richter et al., 2007; S. Singh et al., 2007a, 2007b; Wallach et al., 2020; Zhou et al., 2020). Driven by concerns over increased HF risk, the US Food and Drug Administration (FDA) issued a black box warning that specified an increased risk of HF associated with TZD treatment (Starner et al., 2008). Given that the mechanisms by which TZD may mediate HF remain uncharacterised and that the scope of T2DM management is constantly evolving (e.g. the use of anti-T2DM medications with cardiovascular benefits is increasing), it is imperative to expand our understanding of anti-T2DM agents with potential cardiovascular benefits, including TZD agents (Association, 2023). Understanding how TZDs affect the heart will help improve their safety and efficacy profile and support the selection of cost-effective multi-target medications.

In the past few years, there has been growing interest in adopting toxicoproteomics in mechanistic toxicology (Nguyen et al., 2022; Nury et al., 2023; Thomas et al., 2023). Innovations in bioanalytical platforms used for proteomic analyses, including liquid chromatography coupled with electrospray ionisation mass spectrometry, surface-enhanced laser desorption/ionisation mass spectrometry and matrix-assisted laser desorption/ionisation coupled with time-of-flight mass spectrometry, and the advent of bioinformatics tools are allowing researchers to gain unprecedented insight into protein structure, abundance and interactions, as well as the composition of the proteome and post-translational modifications (Y. Li et al., 2021). In turn, these advances are opening new avenues for the identification of potential toxicity biomarkers and the detection of pathway perturbations resulting from drug treatment (Nguyen et al., 2022). It is evident from the published findings of current toxicoproteomics studies that considerable progress is being made towards the discovery of toxicity biomarkers and that our understanding of the mechanisms that underpin toxicity pathways is improving (Nury et al., 2023; Thomas et al., 2023).

Extending upon our prior research employing toxicometabolomics approach in AC16 cells (Al Sultan et al., 2024), this study aimed to further assess the cardiotoxic effects of TZDs through comprehensively:

1. Investigating the cytotoxic effects of TZDs on the AC16 cardiomyocyte cell line in vitro, and its mechanism of action in terms of PPAR-γ dependency
2. Profiling the biochemical pathways perturbed in TZD-treated AC16 cells using a novel micro-flow liquid chromatography–mass spectrometry (LC–MS)-based toxicoproteomics pipeline. In addition, a weighted correlation network analysis (WGCNA) was performed to further explore the basis of TZD's undesirable off-target mechanisms of action and to identify the driver proteins associated with such effects.

2 | MATERIALS AND METHODS

2.1 | Drugs and chemicals

PGZ, ROSI and the PPAR-γ antagonist GW9662 were purchased from Sigma-Aldrich (St Louis, MO, USA). The TZD agents and GW9662 100 mM stock solutions were prepared in sterile dimethyl sulphoxide (DMSO) (Cat. No. 12611P; Cell Signaling Technology Beverly, MA, USA), and then further diluted to the appropriate half maximal inhibitory (IC_{50}) concentrations with culture medium for in vitro experiments. The final concentration of DMSO in the medium was ≤0.1% (v/v).

The EasyPep Mini MS Sample Prep Kit that was used for the proteomic profiling of cultured cells was purchased from Thermo Fisher Scientific (Cat. No. A40006; Rockford, IL, USA). The following items were included in the kit: lysis solution, universal nuclease, reduction solution, alkylation solution, Pierce™ Trypsin/Lys-C Protease Mix (MS Grade), digestion stop solution, peptide clean-up columns, wash solution A, wash solution B, elution solution and low protein-binding collection tubes. The reagents used for the LC–MS analysis consisted of high-performance liquid chromatography (HPLC)-grade acetonitrile, methanol, analytical-grade formic acid and ultrapure water and were purchased from Fisher Scientific (Loughborough, Leicestershire, UK).

2.2 | Cells and cell culture

The AC16 cell line is derived from adult human ventricular cardiomyocytes and was purchased from Sigma-Aldrich (Product. No. SCC109; St Louis, MO, USA). Cells were cultured in Dulbecco's Modified Eagle's Medium (DMEM/F-12, Product. No. D6434; Sigma-Aldrich, St Louis, MO, USA) supplemented with 12.5% foetal bovine serum, 1% antibiotics (streptomycin and penicillin) and 2 mM L-glutamine at 37°C in a humid atmosphere of 5% CO_2 and 95% air.

TABLE 1 Summary of the key findings of meta-analyses conducted on thiazolidinedione use and its associated cardiovascular effects. Colour shading indicates the following: no significant treatment effect, lower risk and higher risk for grey, green and pink, respectively.

Meta-analysis	Included trials, *n*	TZD under investigation	Treatment duration	CV risk				
				MI	Stroke	All-cause mortality	CV mortality	HF
(Liao et al., 2017)	9 RCTs ($n = 12{,}026$)	PGZ	>52 weeks	RR, 0.8 (95% CI 0.62–1.03; $p = 0.08$)	RR, 0.78 (95% CI 0.60–1.02; $p = 0.07$)	RR, 0.93 (95% CI 0.80–1.09; $p = 0.40$)		RR, 1.32 (95% CI 1.14–1.54; $p = 0.0003$)
(de Jong et al., 2017)	10 RCTs ($n = 10{,}095$)	PGZ	Not within the predefined inclusion criteria	RR, 0.77 (95% CI 0.64–0.93; $p = 0.007$)	RR, 0.81 (95% CI 0.68–0.96; $p = 0.02$)	RR, 0.94 (95% CI 0.81–1.08; $p = 0.38$)		RR, 1.33 (95% CI 1.14–1.54; $p = 0.0002$)
(Zhou et al., 2020)	26 RCTs ($n = 19{,}645$)	PGZ	Not within the predefined inclusion criteria	RR, 0.8[a] (95% CI 0.6–1.0; $p = 0.023$)	RR, 0.8[b] (95% CI 0.7–0.9; $p = 0.018$)	RR, 1 (95% CI 0.8–1.1; $p = 0.64$)	RR, 1 (95% CI 0.7–1.2; $p = 0.67$)	RR, 1.3 (95% CI 1.1–1.6; $p < 0.01$)
(Nissen & Wolski, 2007)	42 RCTs ($n = 27{,}800$)	ROSI	≥24 weeks	OR, 1.43 (95% CI 1.03–1.98; $p = 0.03$)			OR, 1.64 (95% CI 0.98–2.74; $p = 0.06$)	
(Nissen & Wolski, 2010)	56 RCTs ($n = 35{,}531$)	ROSI	≥24 weeks	OR, 1.28 (95% CI 1.02–1.63; $p = 0.04$)			OR, 1.03 (95% CI 0.78–1.36; $p = 0.86$)	
(Wallach et al., 2020)	33 RCTs ($n = 21{,}156$)	ROSI	≥24 weeks	OR, 1.17 (95% CI 0.92–1.51; $p < 0.05$)			OR, 1.15 (95% CI 0.55–2.41; $p < 0.05$)	OR, 1.54 (95% CI 1.14–2.09; $p < 0.05$)
(S. Singh et al., 2007a)	4 RCTs ($n = 14{,}291$)	ROSI	≥52 weeks	RR, 1.42 (95% CI 1.06–1.91; $p = 0.02$)			RR, 0.90 (95% CI 0.63–1.26; $p = 0.53$)	RR, 2.09 (95% CI 1.52–2.88; $p < 0.001$)
(Richter et al., 2007)	18 RCTs ($n = 3888$)	ROSI	≥24 weeks	No evidence				OR, 2.27 (95% CI 1.83–2.81; $p < 0.05$)
(Lago et al., 2007)	7 RCTs ($n = 20{,}191$)	Both agents	Not within the predefined inclusion criteria				RR, 0.93 (95% CI 0.67–1.29; $p = 0.68$)	RR, 1.72 (95% CI 1.21–2.42; $p = 0.002$)
(S. Singh et al., 2007b)	3 RCTs ($n = 20{,}191$)	Both agents	≥24 weeks					OR, 2.1 (95% CI 1.08–4.08; $p = 0.03$)

Abbreviations: CI, confidence interval; CV, cardiovascular; HF, heart failure; MI, myocardial infarction; OR, odds ratio; PGZ, pioglitazone; RCTs, randomised controlled trials; ROSI, rosiglitazone; RR, relative risk; TZD, thiazolidinedione.

[a]Non-fatal MI.

[b]Non-fatal stroke.

2.3 | In vitro cytotoxicity measurements

2.3.1 | Cell viability assay

The cytotoxic effect of TZDs on cardiomyocytes was measured using an MTT [3-(4,5-dimethylthiazol-2-yl)-2,5-diphenyltetrazolium bromide] assay kit (Cat. No. V13154; Thermo Fisher, Eugene, OR, USA). The cells were seeded in 96-well microplates (Cat. No. 655180; Greiner Bio-One, Gillingham, Dorset, UK) (1×10^4 cells/well) and exposed to increasing concentrations of the TZD agent (0.01, 0.1, 0.5, 1, 5, 10 and 20 μM) for 24 h. Following the incubation period, the MTT solution (5 mg/mL) was added to each well, the supernatants were removed and 50 μL of DMSO was used to dissolve the yielded formazan precipitate. A plate reader (GloMax Explorer Multimode Microplate Reader; Promega, Madison, WI, USA) was used to measure the formazan absorbance at 560 nm.

Cell viability was expressed as a percentage and calculated as follows:

$$(\mathrm{A-treatment-A-blank})/(\mathrm{A-control-A-blank}) \times 100\%,$$

where *A* is absorbance. The IC_{50} value was determined from a three-parameter nonlinear regression curve fitted to TZD concentration and the obtained absorbance values using GraphPad Prism 9 software (San Diego, CA, USA).

2.3.2 | Luminescence assay used to detect caspase activity

The activity of caspase 3 and caspase 7 was assessed using a Caspase-Glo 3/7 assay kit (Part No. G8090; Promega, Madison, WI, USA) according to the manufacturer's protocol. Cells were seeded in white-walled 96-well plates (1×10^5 cells/well) and incubated overnight. Following exposure to various concentrations of either PGZ or ROSI (0.01, 0.1, 1, 5, 10 and 20 μM) for 24 h, the cells were lysed by adding 100 μL of the Caspase-Glo 3/7 reagent to each well. Subsequently, equal volumes of the samples and reagent were mixed and incubated for 1 h at room temperature. Luminescence was measured using a plate reader (GloMax Explorer Multimode Microplate Reader). The activity was expressed as relative luminescence units (RLUs) and calculated using the following formula:

$$\mathrm{RLU} = \mathrm{luminescence\,(sample)} - \mathrm{luminescence\,(blank)}.$$

2.3.3 | Measurement of adenosine triphosphate production

The CellTiter-Glo Luminescent Assay (Part No. G7570; Promega, Madison, WI, USA) was used to determine the level of cellular metabolism by measuring adenosine triphosphate (ATP) levels. Cells were seeded in white 96-well microplates (1×10^4 cells/well) and incubated for 24 h. The cells were then exposed to increasing concentrations of PPAR-γ agonist (1, 5, 10, 50 and 100 μM) in the presence or absence of GW9662 (5 μM) and incubated for a further 24 h. Subsequently, 100 μL of the CellTiter-Glo reagent was added to each well and the plates were agitated for 1 min in a shaking incubator. A luminometer (GloMax Explorer Multimode Microplate Reader) was then used to measure the luminescence.

2.4 | LC–MS-based toxicoproteomics analysis

2.4.1 | Protein extraction

AC16 cells were cultured to 70%–80% confluence and seeded at 2×106 cells/well in six-well plates (Cat. No. 140675; Thermo Fisher Scientific, Roskilde, Denmark). Following attachment, the medium was replaced with either fresh medium (control) or medium containing TZD agent at the calculated IC50 and incubated for 24 h. Cells were scraped from the six-well plates, aliquoted into 1.5 mL Eppendorf microtubes (Eppendorf, Hamburg, Germany) and centrifuged at 3000 g for 10 min (4°C). The supernatant was discarded, and cell pellets were retained for proteomics profiling using EasyPep Mini MS Sample Prep Kits in accordance with the manufacturer's instructions as described in Varnavides et al. (2022). In addition to the experimental samples, quality control (QC) and blank samples were prepared. The QC sample was prepared by pooling equal volumes of all the experimental samples, while the blank sample consisted of 50 μL of acetonitrile:water (50:50).

2.4.2 | Micro-flow LC–MS-based proteomics

Peptide separation was performed on a binary Thermo Vanquish ultra-high-performance liquid chromatography system where 20 μL of the reconstituted peptide mixture extract was injected onto a Thermo Acclaim C18 PepMap 100 column (150 mm × 1 mm, particle size 3 μm) and separated over a 100 min method. The column was maintained at 40°C, while the autosampler temperature was set at 5°C. For chromatographic separation, a consistent flow rate of 50 μL/min was used where the mobile phase in positive and negative heated electrospray ionisation mode (HESI±) was composed of Solvent A (99.9% water with 0.1% formic acid) and solvent B (99.9% acetonitrile with 0.1% formic acid). All post columns viper fittings had a 75 μm internal diameter (black colour code).

A high-resolution Exploris 240-Orbitrap mass spectrometer (Thermo Fisher Scientific) was used to perform bottom-up proteomics analysis. Operating parameters were set as follows: spray voltages of 3400 V in HESI +ve mode. The temperature of the ion transfer tube was set at 320°C with a vaporiser temperature of 75°C. Sheath, aux gas and sheath gas flow rates were set at 25, 5 and 0 Arb, respectively. A Top-20 Data-Dependent Acquisition (DDA) was performed

using the following parameters: survey scan range was 275–1500 m/z with MS1 resolution of 120,000, RF lens of 70% and an intensity threshold of 1.0e4. Subsequent MS/MS scans were collected with a resolution of 15,000, an isolation window of 1.2 m/z and a normalised HCD collision energy of 30%. A data-dependent cycle time of 3 s between master scans was also employed. High-purity nitrogen was used as nebulising and as the collision gas for higher energy collisional dissociation.

2.4.3 | Data pre-processing

Using Proteome Discoverer (PD) v3.0 software (Thermo Fisher, San Jose, CA, USA), the MS raw data were used to search the UniProtKB Human Reference Proteome database (v22.07.13; 79,740 entries), including common contaminants (247 entries), using the SEQUEST and Percolator algorithms involved in modified label-free quantification (LFQ) standard processing and consensus workflows. The precursor mass tolerance was set to 10 ppm and 0.02 Da for fragment mass tolerance. Full tryptic digestion was selected, with up to two missed cleavages allowed. The minimum and maximum peptide lengths were set at 6 and 144 amino acids, respectively. Cysteine carbamidomethylation was set as a static modification, and oxidation of methionine (Met), Met loss and N-terminal acetylation were set as dynamic modifications. A maximum of three modifications were allowed per peptide. A concentrated target–decoy approach was applied for the false discovery rate (FDR) calculation, which was set to 1% for highly confident peptide hits.

For protein abundance, the Feature Mapper node was enabled. The raw files were chromatographically aligned with a 10-min retention time shift. The minimum signal-to-noise threshold for feature linking and mapping was set at a value of 5. For precursor peptide abundance, precursor chromatographic intensities were used for precursor quantification results, and the total peptide amount was the selected normalisation mode to correct for experimental bias. Unique and razor peptides were used to quantify the identified proteins.

2.5 | Bioinformatic analyses of toxicoproteomics data

2.5.1 | Dimensionality reduction approaches and identification of DEPs

To capture the underlying uniformity and heterogeneity within the data obtained from the two sample groups, dimensionality reduction and clustering methodologies were performed in R v4.3.0, including principal component analysis (PCA), t-stochastic neighbour embedding (t-SNE) and generation of a hierarchical clustering heatmap. Notably, the *ggbiplot* package (Joon et al., 2023) was used on the linearly transformed data to generate the PCA scatter plot, and two components were extracted. In contrast, the *Rtsne* (Krijthe et al., 2018) and *ggplot2* (Wickham et al., 2016) packages were utilised to perform the nonlinear t-SNE, and the resultant output data were clustered based on the protein expression data. Furthermore, hierarchical clustering analysis, with Euclidean distance as the distance metric and the complete method as the agglomerative clustering algorithm, was performed using the *pheatmap* package (Kolde & Kolde, 2015).

To identify differentially expressed proteins (DEPs), a $\log_2$ fold change (FC) value of 1 and a p-value ≤ 0.05 were set as cutoffs. A volcano plot was accordingly generated to visualise the discriminant proteins using the *ggplot2* package (Wickham et al., 2016).

2.5.2 | GO, DO and KEGG pathway analyses

To acquire a systematic understanding of the biological functions and pathways associated with the identified DEPs, an overrepresentation analysis of the Gene Ontology (GO) and Kyoto Encyclopedia of Genes and Genomes (KEGG) enrichment pathways was performed utilising the *enrichDAVID* function of the *clusterProfiler* package (Yu et al., 2012). Furthermore, mining protein–disease associations have opened a new avenue for exploring protein recruitment from the disease perspective. Therefore, disease ontology (DO) enrichment analysis was also performed using the Genetic Association Database, which is based on the Database for Annotation, Visualization and Integrated Discovery (DAVID; https://david.ncifcrf.gov; v2023q1). The GO, DO and KEGG enrichment terms that had a cumulative hypergeometric p-value < 0.05 and a minimum count of 2 were considered statistically significant.

2.5.3 | WGCNA and module identification

WGCNA is an established analytical co-correlation tool that was originally developed for analysing high-throughput genomic datasets predominantly via unsupervised clustering (Langfelder & Horvath, 2008; Liu et al., 2021). The unsupervised clustering method is used to classify genomic data into biologically meaningful modules of coexpressed genes and can be used to identify regulatory networks, disease-associated modulation in genomic networks and the 'driver genes' that are critical in disease onset and progression (Langfelder & Horvath, 2008; Liu et al., 2021). Recent studies have highlighted the successful deployment of WGCNA in quantitative proteomics (Wu et al., 2021; Zhang et al., 2018). Here, a WGCNA was constructed using the *WGCNA* r-package (Langfelder & Horvath, 2008; Wu et al., 2021) and the entire proteomic dataset excluding the outliers. A similarity matrix was constructed by measuring each pairwise protein correlation and then converted to an adjacency matrix using an appropriate soft threshold power (β) estimated using the *pickSoftThreshold* function (Wu et al., 2021). The obtained adjacency matrix was used to calculate the topology overlap matrix accompanied by the calculation of corresponding dissimilarity (1-TOM). Accordingly, hierarchical clustering based on the distance measure (1-TOM) was performed to generate a clustering dendrogram. Using the dynamic tree-cut algorithm, dendrogram branches with similar co-expression were clustered into

several modules, each assigned a different colour, and the parameter value of the minimum cluster size was set to 30. Lastly, module–trait correlation analysis was conducted to correlate the modules with the TZD-treated samples that potentially had a 'high HF risk' compared with the control samples that had a 'low HF risk'. Only modules with a significant positive correlation with high HF risk were subjected to subsequent analysis (WGCNA's module–GO, DO and KEGG pathway analyses).

2.5.4 | Protein–protein interactions of the key module proteins and identification of hub proteins

The list of identified proteins was uploaded to the Search Tool for the Retrieval of Interacting Genes/Proteins (STRING; https://string-db.org; v11.5) database to generate a full protein–protein interaction (PPI) STRING network limited to *Homo sapiens* with the highest confidence interaction score of 0.9. The developed network was exported to the Cytoscape software platform for visualisation (Cytoscape; https://cytoscape.org; v3.10.1). The cytoHubba plugin in Cytoscape, which provided topological algorithms for ranking nodes, was used to identify the top 20 proteins. Proteins that were cytoHubba-identified driver proteins as well as enriched in pathways linked with HF pathogenesis from both the DEPs and WGCNA KEGG analyses were labelled in this study as feature proteins.

2.6 | Statistical analysis

Statistical analysis was conducted using R v4.3.0. Cytotoxicity data are expressed as mean ± SD. At least three independent experiments were performed for each cytotoxicity assay, with three or more technical replicates for each experimental group tested. Furthermore, three independent experiments were performed for each toxicoproteomics analysis. Statistical significance was determined using Student's or Welch's *t*-tests when comparing the two groups. A non-repeated one-way analysis of variance (ANOVA), followed by Dunnett's post hoc test, was used for multiple comparisons. The correlation coefficient was assessed using Pearson and distance correlation analyses. A p-value ≤ 0.05 was considered statistically significant.

3 | RESULTS

3.1 | In vitro characterisation of TZD cytotoxicity against AC16

3.1.1 | Effects of TZDs on cell viability

The effects of PGZ and ROSI on cell viability were assessed using the MTT assay. AC16 cells were treated with a wide range of concentrations of either TZD agents (0.01, 0.1, 0.5, 1, 5, 10 and 20 μM), and the cytotoxic effect was measured after a 24-h incubation period. As shown in Figure 1A,B, exposure to either TZD resulted in a concentration-dependent decrease in cell viability, and the IC_{50} value against AC16 cells, calculated using the Hill equation (Goutelle et al., 2008), was found to be 4.74 μM ($R^2 = 0.9969$; 95% CI 3.842–5.894) and 2.05 μM ($R^2 = 0.9816$; 95% CI 1.270–3.495) in PGZ and ROSI, respectively.

3.1.2 | Effect of TZDs on caspase 3/7 activity

To investigate the molecular mechanisms underlying the TZD-induced loss of cell viability, we first determined whether apoptosis occurred by measuring caspase 3/7 activity—a gold standard measure of apoptosis (Niles et al., 2008). This assay produces a luminescent substrate that has a four-peptide sequence, which, after cleavage by caspase 3/7, generates a light signal produced by luciferase (Niles et al., 2008). As shown in Figure 1C, the caspase 3/7 activity of the PGZ-treated cells was significantly lower than that of the control cells. This was observed at all PGZ concentrations. However, the activation of caspase 3/7 activity was observed in ROSI-treated AC16 cells that reached significance at 0.01, 0.1, 1, 5, 10 and 20 μM (Figure 1D).

3.1.3 | Involvement of PPAR-γ in TZDs' effects on cell viability

Figure 1E,F shows the effects of TZD on mitochondrial ATP production and the involvement of PPAR-γ in TZD-induced cell death, respectively. The administration of PGZ or ROSI markedly depleted mitochondrial ATP production in AC16 cells in a concentration-dependent manner.

Interestingly, the co-administration of TZDs and PPAR-γ antagonist GW9662 (5 μM) resulted in multi-faceted effects (Figure S1). The presence of GW9662 partially attenuated the cytotoxic effect of PGZ on AC16 cells. Nevertheless, its presence worsened the cytotoxicity of ROSI by further diminishing ATP levels, which aggravated cellular death.

3.2 | Shotgun toxicoproteomics and protein-based bioinformatics analyses of TZD-treated human AC16 cells

3.2.1 | Characterisation of the proteome of TZD-treated human AC16 cells

To characterise the proteins and the mechanism(s) of action underlying the cardiotoxic activity of TZDs and identify the implicated targets, a label-free quantitative proteomic pipeline was applied, as depicted in Figure 2. After processing the raw data of the tryptic peptides using proteome discoverer (PD), further data filtering (false discovery rate < 1% for both peptides and proteins), normalisation and imputation were conducted via NormalyzerDE (Willforss et al., 2018)

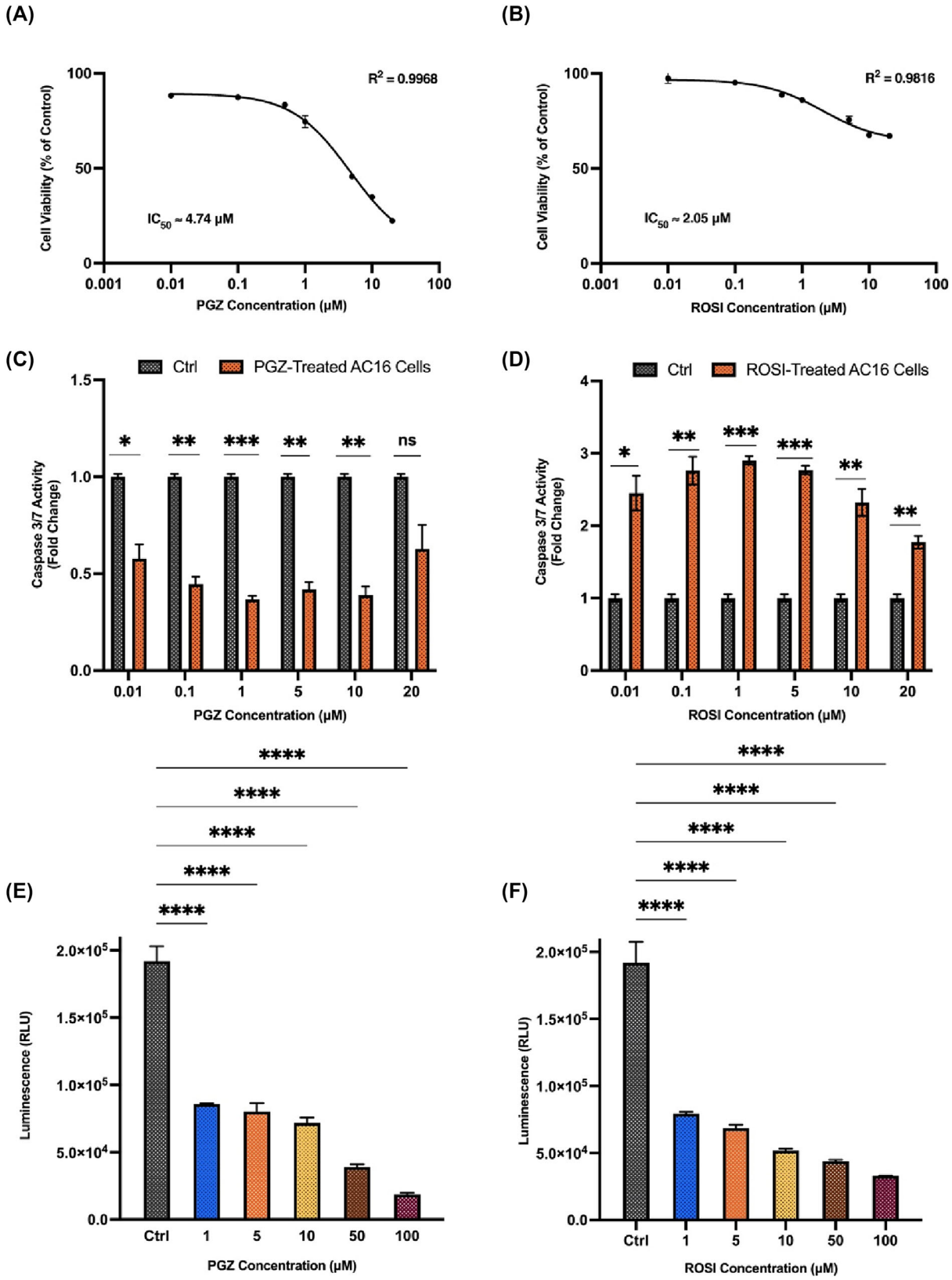

FIGURE 1 Legend on next page.

FIGURE 1 Characterisation of the cytotoxic effect of thiazolidinediones (TZDs) on AC16 cells. Concentration-response modelling and corresponding half maximal inhibitory (IC_{50}) values for pioglitazone (PGZ) (A) and rosiglitazone (ROSI) exposure (B) in AC16 cells. In each experiment, cells were pre-cultured for 24 h in 96-well plates (1×10^4 cells/well) and incubated with increasing concentrations of either PGZ or ROSI for another 24 h. Each point is the average of four independent experiments (each in quadruplicate), with the standard deviation indicated by error bars. (C, D) The effect of TZDs on caspase 3/7 activity. The fold change in the *y*-axis represents the level of caspase 3/7 activity in the TZD-treated AC16 cells relative to that of the control group. The data are from three independent experiments, each performed in triplicate, and expressed as mean ± SD. Statistical significance was assessed using the Student's *t* test (each concentration of TZD vs. the control). The effect of the TZDs on mitochondrial adenosine triphosphate (ATP) production and quantifying cellular ATP production levels of AC16 cells after 24 h of exposure to increasing concentrations of either PGZ (E) or ROSI (F) using the CellTiter-Glo luminescent assay are shown. The data are from three independent experiments, each performed in triplicate, and expressed as mean ± SD. Statistical significance was determined using one-way analysis of variance (ANOVA) and Dunnett's multiple-comparisons test (the control vs. each concentration of TZD). $^{*}p < 0.05$; $^{**}p < 0.01$; $^{***}p < 0.001$; $^{****}p < 0.0001$.

and NAguideR (S. Wang et al., 2020) packages, yielding thousands of proteins in both PGZ and ROSI experiments.

Various chemometric analyses were performed to profile TZD-induced, proteome-wide changes in expression in AC16 cells. In both experiments, the multivariate PCA technique was employed to visualise the heterogeneity in the expression data among the studied samples. The PCA scores plots revealed that the control and PGZ-treated samples, shown in Figure 3A, and the control and ROSI-treated samples (Figure 3B), were distinct. Nevertheless, PCA analysis identified samples labelled Drug-2 (PGZ) and Drug-7 (ROSI) as potential outliers and therefore, these samples were excluded from further analyses. Distinct proteomic profiles differentiating control and treated groups were further validated following the application of t-SNE; sample separation was also achieved using the first two t-SNE components (Figure 3C,D). To discern the protein expression trends of the two studied genotypes globally, another t-SNE plot was generated in which the quantified proteins were projected into the t-SNE space and clustered accordingly based on their expression patterns. The t-SNE plot in Figure 3E,F shows the expression-driven separation of the control and treated groups and highlights the downregulation trend observed in a large set of proteins following the treatment of cells with the TZD agent. To capture the DEPs responsible for the separation and clustering observed in the PCA and t-SNE results, a volcano plot was generated using data that fell under the threshold values ($\log_2$FC > 1 and $p \leq 0.05$), and 237 upregulated and 368 downregulated proteins were identified after PGZ exposure (Figure S2A). Proteins significantly affected after ROSI exposure yielded 198 significant proteins (97 upregulated and 101 downregulated), as shown in Figure S2B.

3.2.2 | Functional, disease and pathway analyses of the DEPs

To gain insights into the implicated molecular mechanisms and further delineate the cellular responses to TZD treatment, GO, DO and KEGG pathway analyses of the DEPs were performed.

Regarding PGZ exposure, the GO enrichment analysis based on biological process (BP) revealed that the DEPs were associated with various processes, including intermediate filament organisation, oxygen transport, blood coagulation, the mitogen-activated protein kinase (MAPK) cascade and mitochondrial translation (Figure 4A). Furthermore, the DEPs were found to be markedly enriched in molecular functions (MFs) associated with protein binding, haptoglobin binding, oxygen transporter activity and extracellular matrix (ECM) structural constituents (Figure 4A). Parallel to the BP and MF analysis findings, the DEPs were overrepresented in compartments, including the cytosol, extracellular exosome and cytoplasm (Figure 4A). In response to ROSI treatment, the GO functional analyses showed that the DEPs were predominantly assembled into BP linked to nucleosome assembly, intermediate filament organisation, protein folding, telomere organisation, innate immune response in mucosa and Rab protein signal transduction (Figure 4B). On the MF level, the DEPs were mainly involved in structural constituents of chromatin, RNA binding, protein heterodimerization activity, ATPase activity, nucleosomal DNA binding and DNA binding (Figure 4B). On the cellular component (CC) levels, the DEPs were predominantly localised in the nucleosome, cytosol, blood microparticle, membrane, nuclear chromosome and nucleus (Figure 4B).

The DO analysis revealed that the PGZ's DEPs were predominantly associated with cardiovascular diseases (CVDs), such as atherosclerotic CVD, myocardial infarction (MI), peripheral (i.e. venous thromboembolism) and cerebrovascular (i.e. stroke) diseases (Figure S3A). Interestingly, as shown in Figure S3A, 103 DEPs were enriched in the DO termed 'type 2 diabetes-oedema-rosiglitazone'. This finding could potentially explain the worsening body congestion noted in diabetic patients who use PGZ as part of their treatment, as evidenced in numerous case reports (De Flines & Scheen, 2007). However, the DO enrichment analysis of the DEPs induced by ROSI revealed their implications in various diseases, including blood disorders (glucosephosphate dehydrogenase deficiency, sickle cell anaemia), neurodegenerative disorders (e.g. Alzheimer's disease, Parkinson's disease) and peripheral diseases, such as venous thrombosis. Similar to PGZ's DO findings, the majority of DEPs were markedly enriched in the DO termed 'type 2 diabetes-oedema-rosiglitazone', signifying the implication of oedema in cardiotoxicity pathogenesis (Figure S3B).

The KEGG pathway analysis revealed 37 enriched pathways that fulfilled the applied criteria of a *p*-value < 0.05 and a minimum count of 2 (Figure 4C). The KEGG pathway analysis findings also showed

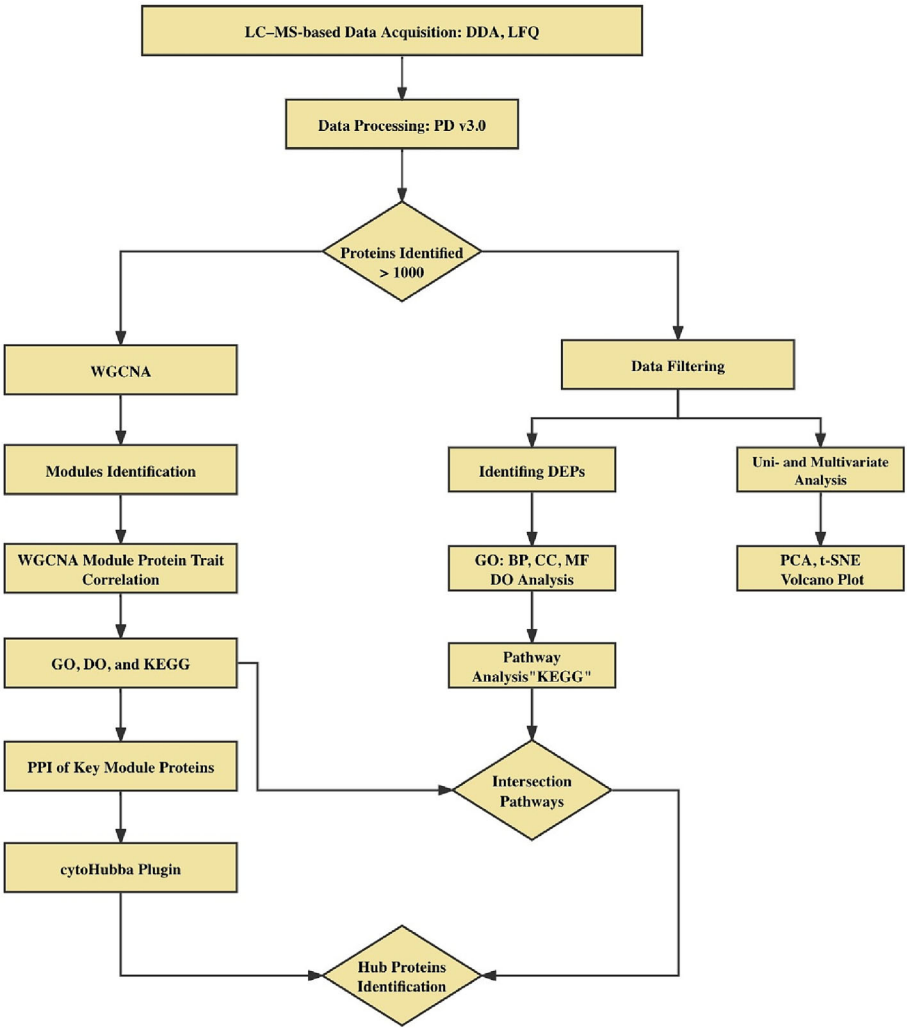

FIGURE 2 Flowchart of the toxicoproteomics pipeline used in this study for the downstream analyses. The total proteome of the AC16 cells produced in response to thiazolidinedione (TZD) was characterised using a novel microflow label-free shotgun toxicoproteomics approach. Initially, the raw liquid chromatography–mass spectrometry (LC–MS) data were processed using proteome discoverer (PD), followed by further data filtering, normalisation and imputation, yielding a total of >1000 proteins in each experiment. Accordingly, downstream analysis, represented by uni- and multi-variate analyses, was performed on the identified proteins. Weighted correlation network analysis (WGCNA) was conducted on all identified proteins. In parallel to WGCNA, the differentially expressed proteins (DEPs) under the threshold values ($\log_2$FC > 1 and $p \leq 0.05$) were captured. Further functional (Gene Ontology [GO]), disease (disease ontology [DO]) and pathway (Kyoto Encyclopedia of Genes and Genomes [KEGG]) analyses of both the WGCNA results and DEPs were performed. The pathways significantly implicated in heart failure (HF) pathogenesis, which were identified from the examination of the DEPs and the WGCNA, were intersected. The key module proteins extracted from the WGCNA were mapped to the protein–protein interaction (PPI) network, and then the top 20 driver proteins were identified using the cytoHubba plugin. Finally, proteins that were cytoHubba-identified driver proteins as well as enriched in pathways linked with HF pathogenesis from both the DEPs and WGCNA KEGG analyses were labelled in this study as feature proteins. BP, biological process; CC, cellular component; DDA, data-dependent acquisition; LFQ, label-free quantitation; MF, molecular function; PCA, principal component analysis; t-SNE, t-stochastic neighbour embedding.

that the screened proteins were associated with pathways primarily involved in immune-related cellular processes and signal transduction-based pathways, which include the complement and coagulation cascades (KEGG: 04610), platelet activation (KEGG: 04611), neutrophil extracellular trap formation (KEGG: 04613), the Wingless-related integration site (Wnt) signalling pathway (KEGG: 04310), the phosphatidylinositol 3′ kinase-protein kinase B (PI3K-Akt) signalling pathway (KEGG: 04151), ECM-receptor interaction (KEGG: 04512), focal adhesion (FA) (KEGG: 04510) and the regulation of the actin cytoskeleton (KEGG: 04810). The pathway-topology analysis (Figure 4D) of the proteins markedly altered in response to ROSI showed a significant association between the DEPs and pathways linked to immune-related systems (i.e. neutrophil extracellular trap formation (KEGG: 04613)), circulatory system and CVD (e.g. cardiac muscle contraction (KEGG: 04260), diabetic cardiomyopathy (KEGG: 05415)) and excretory system (e.g. endocrine and other factor-regulated calcium reabsorption (KEGG: 04961), proximal tubule bicarbonate reclamation (KEGG: 04964) and collecting duct acid secretion (KEGG: 04966)).

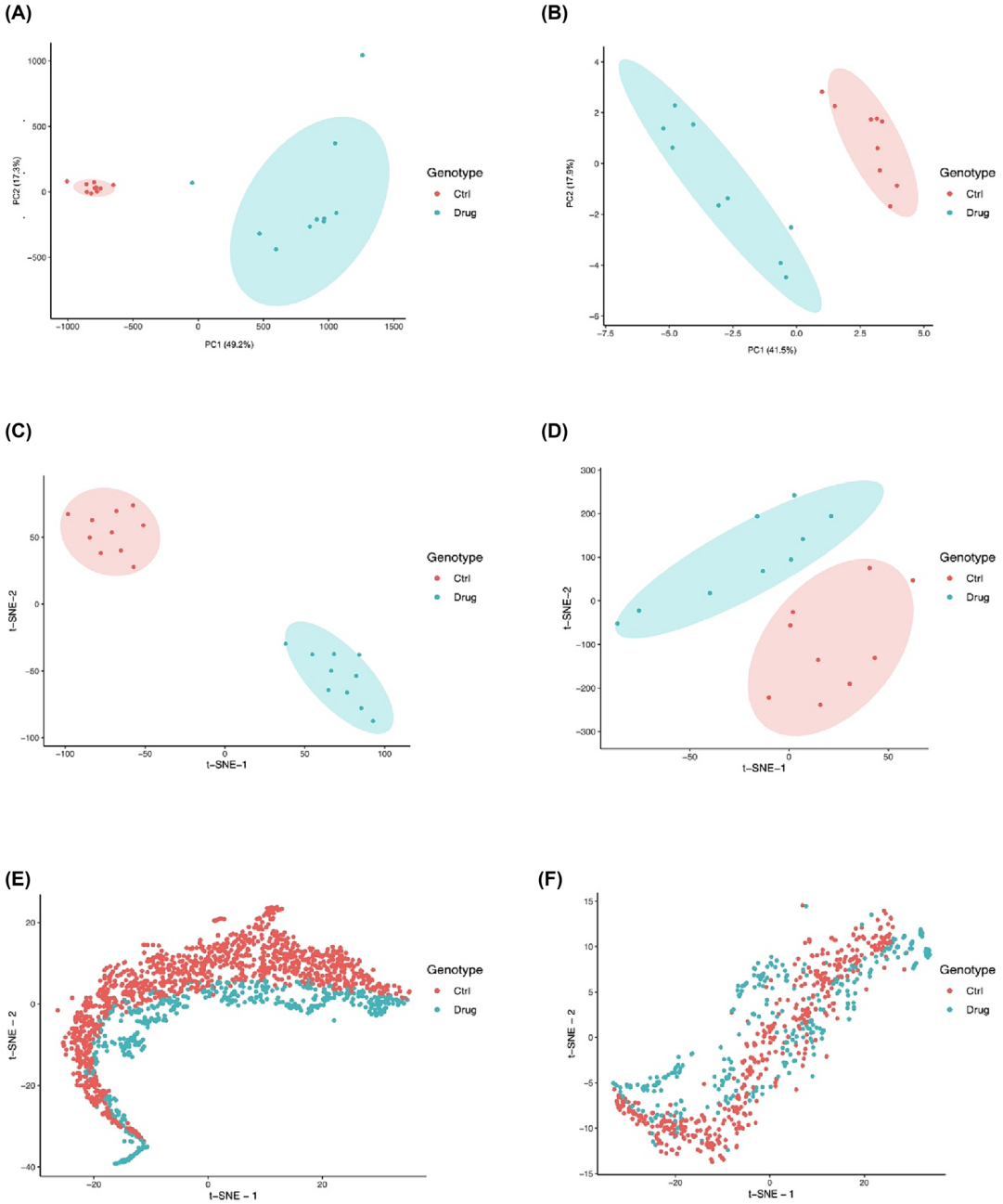

FIGURE 3 Chemometric analyses of proteomics data. (A, B) 2D principal component analysis (PCA) scores plots showing the trend of separation between the control and thiazolidinedione (TZD)-treated groups. (A) The PCA scores plot visualises the separation between control and pioglitazone (PGZ)-treated samples based on the principal components (PCs) that capture the most variance in the data. (B) The PCA scores plot depicts the separation between control and rosiglitazone (ROSI)-treated samples based on the first two PCs (PC1 and PC2). (C, D) t-stochastic neighbour embedding (t-SNE) plots visualising the distribution of control and TZD-treated samples based on their protein expression profiles. The t-SNE algorithm projects high-dimensional data into a lower-dimensional space (2D) for better visualisation. Plot (C) illustrates the distinct separation between PGZ-treated and control cells, while plot (D) demonstrates the separation between ROSI-treated and control samples, as observed in their protein expression profiles. The discernible separation between the control and TZD-treated cell populations depicted in plots (C) and (D) indicates unique protein expression patterns induced by the TZD treatment. In both C and D, the *Rtsne* values used were $Perp = 5$, $\eta = 200$ and $T = 5000$. The shaded circles in plots A–D represent 95% confidence intervals, while the coloured dots illustrate the individual samples. (E, F) Clustered protein visualised within t-SNE across samples on the basis of expression. (E, F) Proteome datasets of PGZ and ROSI, respectively. In both E and F, the *Rtsne* values applied were $Perp = 50$, $\eta = 200$ and $T = 5000$. DEPs, differentially expressed proteins; LC–MS, liquid chromatography–mass spectrometry; $Perp$, perplexity; T, maximum number of iteration; η, learning rate.

Furthermore, the KEGG analysis revealed the involvement of DEPs in pathways related to the following: carbohydrate metabolism (i.e. glycolysis/gluconeogenesis [KEGG: 00010]), citrate cycle (TCA cycle [KEGG: 00020], pyruvate metabolism [KEGG: 00620]), energy

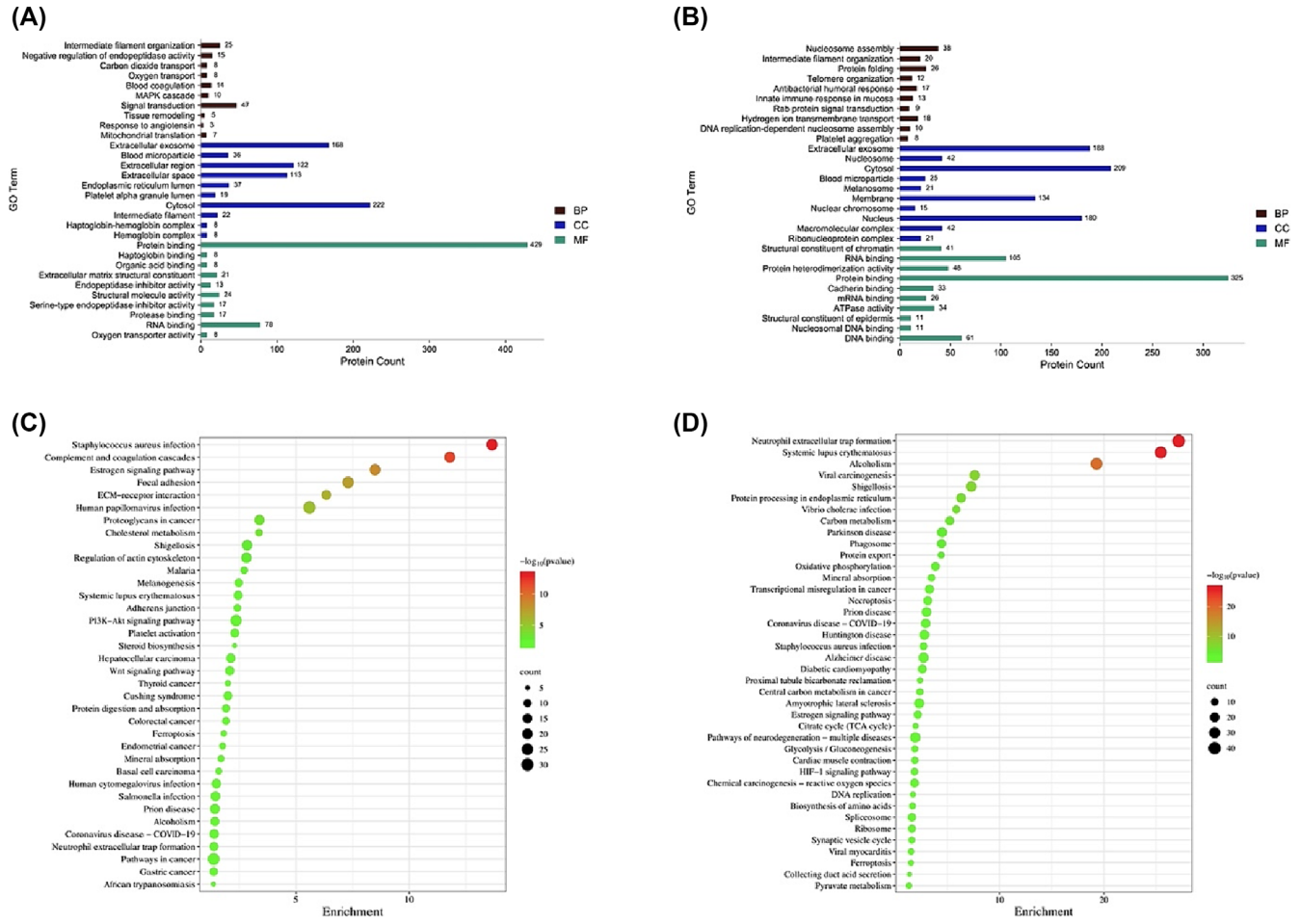

FIGURE 4 Functional and pathway analyses of the differentially expressed proteins (DEPs). The top 10 enriched Gene Ontology (GO) terms for the biological process (BP), cellular component (CC) and molecular function (MF) categories of the DEPs of pioglitazone (PGZ) (A) and rosiglitazone (ROSI) (B). In panels (A, B), the *x*-axis represents the number of DEPs, while the *y*-axis shows the GO annotation terms. The bubble plots in C and D list all the significantly enriched pathways of the DEPs of PGZ and ROSI, respectively. In C and D, the bubble size and colour represent the number of DEPs enriched in the pathway and the enrichment significance, respectively. KEGG, Kyoto Encyclopedia of Genes and Genomes.

metabolism (i.e. oxidative phosphorylation [KEGG: 00190]) and cellular processes (i.e. phagosome [KEGG: 04145], ferroptosis [KEGG: 04216], necroptosis [KEGG: 04217]).

3.2.3 | WGCNA and module identification

A WGCNA was constructed using a PGZ dataset that included 19 samples by adopting the WGCNA package. To ensure a scale-free network, a soft threshold power ($\beta = 8$; scale-free $R^2 = 0.85$) was selected as shown in Figure S4A,B, yielding four protein co-expression modules (blue, yellow, turquoise and brown), which ranged in size from 60 to 904 proteins (Figure 5A). To achieve a clear understanding of the molecular changes that occur in AC16 cells following PGZ treatment, a module–trait correlation analysis was conducted to correlate the identified modules with the PGZ-treated samples that potentially had a 'high HF risk' compared with the control samples that had a 'low HF risk'. It was found that only the blue module demonstrated a strong positive correlation with the high-HF-risk samples (correlation coefficient = 0.964, $p < 0.001$) (Figure 5B). An intramodular analysis demonstrating the correlation between blue module members (MMs) and protein significance for the chosen trait is illustrated in Figure S5.

Regarding the ROSI dataset, a soft-threshold power of 8 was selected on the basis of the scale-free fit index and mean connectivity values illustrated in Figure S6A,B ($\beta = 8$; scale-free $R^2 = 0.85$). The WGCNA algorithm clustered proteins into eight co-expression modules, which were blue, turquoise, black, red, brown, green, pink and yellow modules, ranging in size from 45 to 148 proteins (Figure 5C). In regard to module–trait correlation analysis, the brown module showed the highest positive correlation with the high-HF-risk samples, with a correlation coefficient value of (correlation coefficient = 0.701, $p < 0.05$) (Figure 5D). A scatter plot of brown MMs versus protein significance is shown in Figure S7.

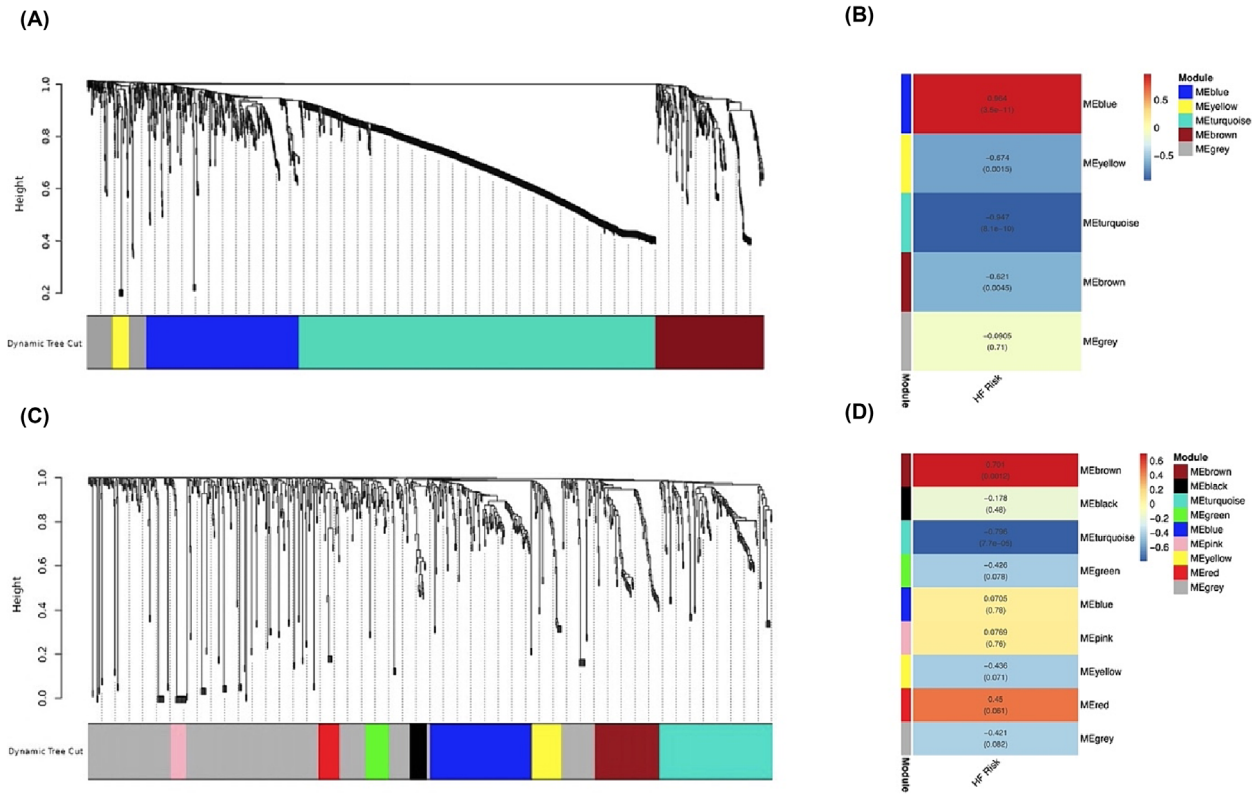

FIGURE 5 Analysis of the protein coexpression modules. Dendrogram of all the identified pioglitazone (PGZ) (A) and rosiglitazone (ROSI) (C) proteins, with dissimilarity clustered on the topological overlap. In (A, C), hierarchical cluster tree showing co-expression modules identified by weighted correlation network analysis (WGCNA). Each branch in the tree represents one protein. The major tree branches constitute four and eight modules, in PGZ and ROSI datasets, respectively, labelled with different colours. (B, D) Diagram showing the correlation between each identified module and the heart failure (HF)-risk trait.

3.2.4 | Functional, disease and pathway analyses of the chosen modules

Given that only the blue and brown modules demonstrated a positive correlation with HF risk in the PGZ and ROSI datasets, additional GO, DO and KEGG enrichment analyses were performed with these modules to further characterise the biological relevance of the MMs and their roles in pathway and disease processes.

Biological inferences of the blue module–PGZ

The GO enrichment analysis revealed that the blue MMs were associated with BPs linked to nucleosome assembly, fibrin clot formation, mitochondrial ATP synthesis and the tricarboxylic acid cycle (Figure 6A). In terms of MFs, the blue MMs were implicated in protein binding, RNA binding, ATPase activity, haptoglobin binding and calcium-ion binding (Figure 6A). The analysis also revealed that most of the blue MMs were localised in the extracellular exosome, cytosol, mitochondria and nucleus (Figure 6A).

The DO enrichment analysis revealed that the blue MMs were primarily associated with the same heart diseases associated with DEPs and other lipid disorders (Figure S8A). It was also found that 86 blue MMs were enriched for 'type 2 diabetes-oedema-rosiglitazone', which was consistent with the results of the DO enrichment analysis of the full set of DEPs.

The KEGG pathway analysis revealed that the blue MMs were significantly enriched in pathways related to CVDs, the immune system, cellular processes and energy metabolism. The immune-related pathways included the complement and coagulation cascades (KEGG: 04610), platelet activation (KEGG: 04611) and neutrophil extracellular trap formation (KEGG: 04613). The CVD-related pathways included diabetic cardiomyopathy (KEGG: 05415) and lipid and atherosclerosis (KEGG: 05417). The cellular processes-related pathways included ferroptosis (KEGG: 04216), necroptosis (KEGG: 04217), the phagosome (KEGG: 04145), the ECM-receptor interaction (KEGG: 04512), FA (KEGG: 04510) and the regulation of the actin cytoskeleton (KEGG: 04810). The energy metabolism-related pathway was the oxidative phosphorylation pathway (KEGG: 00190) (Figure 6C).

Biological inferences of the brown module–ROSI

The GO functional analysis of the brown MMs (Figure 6B) revealed their implication in BPs associated with cellular oxidant detoxification, hydrogen peroxide catabolic process, cytoplasmic translation, negative regulation of growth and intermediate filament organisation. In addition, the brown MMs were markedly enriched in MFs related to endopeptidase inhibitor activity, organic acid binding, serine-type endopeptidase inhibitor activity, oxygen transporter activity and oxygen binding. The proteins in the brown module were found to be predominantly localised in the extracellular exosome, blood microparticle,

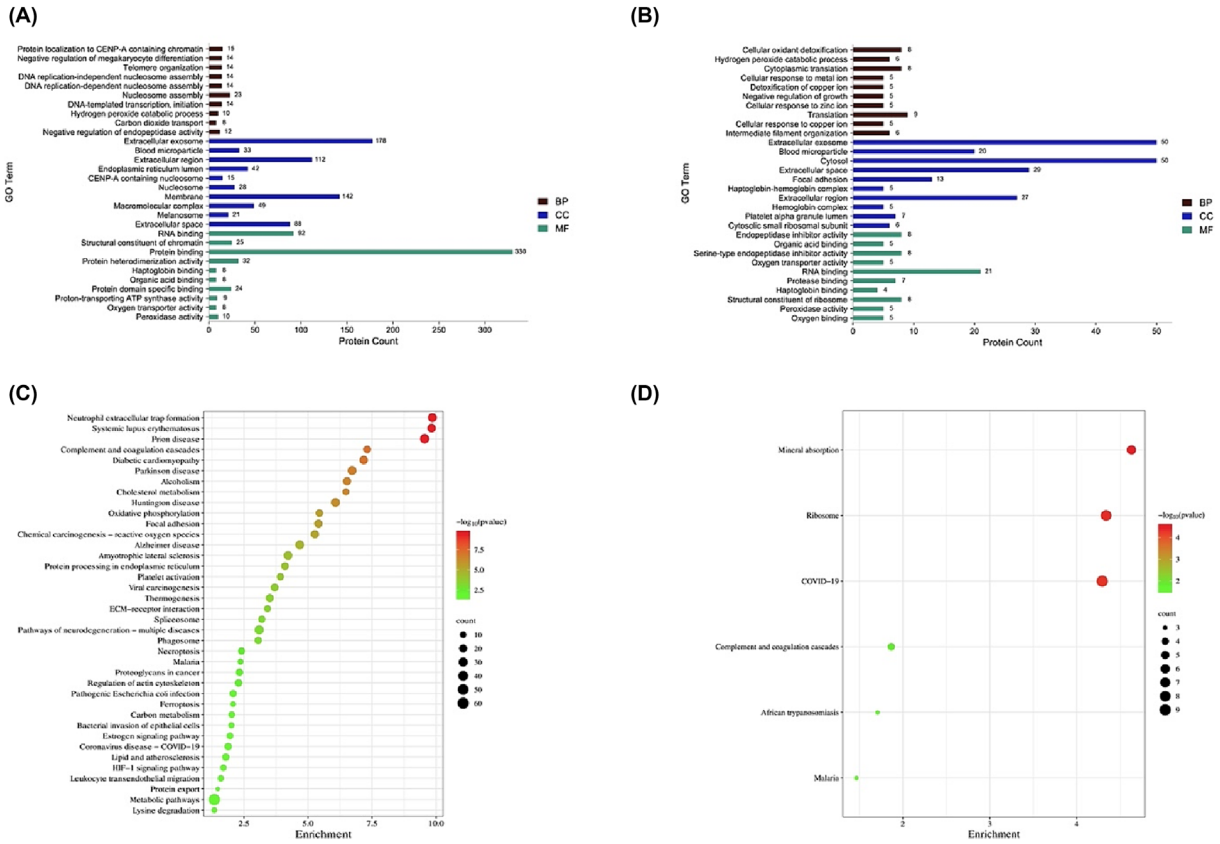

FIGURE 6 Functional and pathway analyses of the members of the chosen modules. The top 10 enriched Gene Ontology (GO) terms for the biological process (BP), cellular component (CC) and molecular function (MF) categories of blue module members (MMs)–pioglitazone (PGZ) (A) and brown MMs–rosiglitazone (ROSI) (B). In panels (A, B), the *x*-axis represents the number of MMs, while the *y*-axis shows the GO annotation terms. The bubble plots in C and D list all the enriched pathways of the protein members of the blue and brown modules, respectively. In C and D, the bubble size and colour represent the number of proteins enriched in the pathway and the enrichment significance, respectively. KEGG, Kyoto Encyclopedia of Genes and Genomes.

cytosol, extracellular space, FA, haptoglobin–haemoglobin complex and extracellular regions.

Regarding the DO ontology, the proteins in the brown module were mainly enriched in blood disorders (i.e. α-thalassemia, β-Thalassemia, anaemia), dyslipidaemias and neurodegenerative disorders, including Alzheimer's disease. Interestingly, consistent with the findings for PGZ, 'type 2 diabetes-oedema-rosiglitazone' was also enriched (Figure S8B).

Lastly, KEGG pathway enrichment analysis suggested that 133 proteins in the brown module were significantly enriched in the following pathways: mineral absorption (KEGG: 04978), ribosome (KEGG: 03010), and complement and coagulation cascades (KEGG: 04610) (Figure 6D).

3.2.5 | WGCNA and identification of hub proteins

To further identify the key proteins (prognostic biomarkers) implicated in the pathoetiology of TZD use and HF risk, the pathways significantly implicated in HF pathogenesis, which were identified from the examination of the DEPs and the WGCNA, intersected. In the PGZ dataset, this resulted in the identification of seven pathways: the complement and coagulation cascades (KEGG: 04610), platelet activation (KEGG: 04611), neutrophil extracellular trap formation (KEGG: 04613), ferroptosis (KEGG: 04216), the ECM-receptor interaction (KEGG: 04512), FA (KEGG: 04510) and the regulation of the actin cytoskeleton (KEGG: 04810) (Figure 7A). In the context of the ROSI dataset, two pathways were identified: mineral absorption (KEGG: 04978) and ribosome (KEGG: 03010) (Figure 7C).

Subsequently, the hub proteins of each chosen module (blue module–PGZ; brown module–ROSI) were extracted. The MMs were mapped to the PPI network, and then the top 20 driver proteins were identified using the cytoHubba plugin. Brief descriptions of the identified top 20 driver proteins for each module, as well as their expression levels, are summarised in Figure 7B, Table S1, Figure 7D, and Table S2 for the blue and brown modules, respectively.

With respect to the blue module–PGZ, among the 20 listed proteins, eight (P60709, P05556, P00533, P02751, P00734, P21796, P02679 and P02452) intersected with the proteins enriched in the seven pathways (DEPs and WGCNA) mentioned above and were

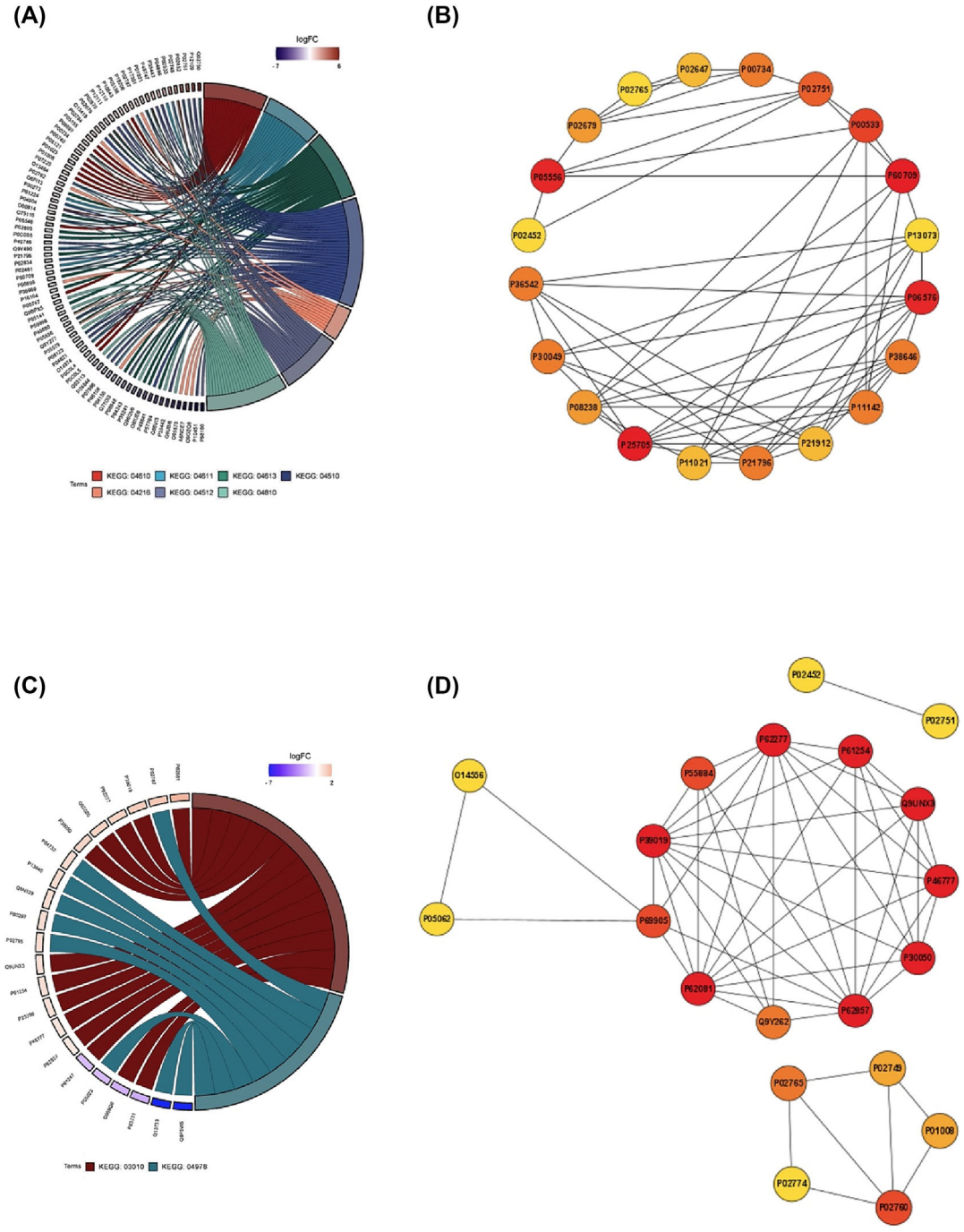

FIGURE 7 Chord diagrams and identification of hub proteins. The common pathways enriched with both the differentially expressed proteins (DEPs) of pioglitazone (PGZ) and blue module members (MMs)–PGZ and the DEPs of rosiglitazone (ROSI) and brown MMs–ROSI are presented in plots A and C, respectively. The top 20 hub proteins in the blue module (B) and brown module (D) identified using Cytoscape's cytoHubba plugin. The node colour denotes the ranking score (red = high score, orange = intermediate score and yellow = low score). KEGG, Kyoto Encyclopedia of Genes and Genomes.

therefore labelled as feature proteins. For brown module–ROSI, eight proteins, which were P30050, Q9UNX3, P61254, P46777, P62277, P39019, P62857 and P62081, were also found to fulfil the proposed criteria and hence recognised as feature proteins.

4 | DISCUSSION

TZDs are a class of antidiabetic agents approved for the management of T2DM. Besides their well-recognised capability in improving insulin

sensitivity, TZDs have been shown to exert multiple pleiotropic effects, including anti-inflammatory, potential neuroprotective and blood pressure-lowering effects (DeFronzo et al., 2013). These pleiotropic actions have extended TZDs' therapeutic horizons beyond glycaemic control and encouraged their application in managing T2DM and its related complications (DeFronzo et al., 2013). Nevertheless, the widespread use of TZDs in clinical practice has shortly been hampered following reports of HF cases associated with their usage (De Flines & Scheen, 2007). Owing to the uncharacterised mechanisms underpinning TZD-induced HF, TZD agents have failed to garner widespread clinical interest, and further exploration of their pleiotropic effects has been hindered, resulting in their gradual disappearance from the realm of active research.

Emerging evidence implicates mitochondrial dysfunction as a potential determinant for the unfavourable effects of various off-target medications (Vuda & Kamath, 2016). Interestingly, a previous paper suggested that mitochondrial dysfunction may be responsible for the cardiotoxic effects of TZDs (Zhong et al., 2018). Hence, to gain deeper insight into this specific potential effect, the cytotoxicity of TZDs on AC16 cells was characterised using three distinct mitochondrial assays and further investigated by undergoing a comprehensive toxicoproteomics approach.

4.1 | Converging pathways to cardiotoxicity: unravelling the shared molecular signatures of PGZ and ROSI

4.1.1 | Distorted cardiac energetics and mitochondrial dysfunction

The MTT assay findings revealed concentration-dependent cytotoxicity of TZDs against AC16 cells, with high potency indicated by low IC_{50} values. Our findings align with prior studies demonstrating dose-dependent loss of viability in rat cardiomyocytes following PGZ treatment (Zhong et al., 2018) and ROSI exposure (Mishra et al., 2014). These cytotoxic effects potentially indicate a mitochondrial involvement in TZDs' cytotoxicity, as the MTT assay relies on mitochondrial respiration (mitochondrial succinate dehydrogenase) for the enzymatic reduction of MTT to the MTT-formazan product (Ghasemi et al., 2023). The role of mitochondrial dysfunction in TZD-induced cardiotoxicity was examined further by measuring the effect of TZDs on mitochondrial ATP production. Consistent with the aforementioned MTT assay findings, TZD treatment resulted in a significant decline in ATP production. Notably, this reduction remained evident following the introduction of the PPAR-γ antagonist GW9662, implying the existence of PPAR-γ-independent mechanisms governing TZD-mediated perturbations in mitochondrial energy production. While the precise mechanisms underlying the observed mitochondrial dysfunction remain complex, our toxicoproteomics analysis revealed a marked downregulation of key pathways implicated in mitochondrial energetics in both TZD treatments. These pathways included oxidative phosphorylation, the citric acid cycle (TCA cycle), and pyruvate metabolism. However, the signalling pathways underpinning these processes revealed a striking divergence between PGZ and ROSI.

With regard to PGZ, the results suggested that the treated cells exhibited mitochondrial uncoupling, represented by significant upregulation of uncoupling proteins referred to as adenine nucleotide translocators (ANTs), including ANT2. Beyond ANTs' well-recognised role in mitochondrial energy output, ANTs also exhibit uncoupling properties, as reported by Busiello et al. (2015) and Demine et al. (2019). Interestingly, a recent study performed with isolated rat liver mitochondria supported the ability of PGZ to induce ANT-mediated uncoupling, as described in Kharechkina et al. (2021).

With respect to ROSI, our analysis revealed a significant perturbation in crucial proteins involved in the oxidation of pyruvate and the citric acid cycle. For instance, a marked downregulation of fumarate hydratase (FH), the homotetrameric mitochondrial enzyme that catalyses the reversible hydration of fumarate to malate as a step in the citric acid cycle (Valcarcel-Jimenez & Frezza, 2023), was associated with ROSI-treated cells. Another perturbated protein in response to ROSI treatment and crucially involved in the pyruvate and citric acid cycle was malate dehydrogenase, a member of the malate–aspartate shuttle (Ahn et al., 2020). The primary role of malate dehydrogenase is to catalyse the reversible conversion of malate to oxaloacetate, facilitating the transfer of NADH from the cytoplasm to mitochondria (Ahn et al., 2020). Hence, with the recognition of the malate dehydrogenase role, its perturbation markedly disrupts the malate–aspartate shuttle, leading to reduced NADH transfer to the mitochondria and thus compromising oxidative phosphorylation. The influence of ROSI on oxidative phosphorylation also reverberates by modulating the expression of mitochondrial complexes, the driving force of mitochondrial ATP production. The treatment of ROSI is associated with the downregulation of human ubiquinol-cytochrome c reductase core protein 1 (UQCRC1), a vital subunit of the mitochondrial complex III (Yi et al., 2020). The UQCRC1 protein plays an essential role in the catalytic activity of complex III, serving as a key facilitator of electron transport from ubiquinol to cytochrome c, thus contributing to the overall functionality of complex III (Yi et al., 2020). Hence, the downregulation of this vital subunit could dramatically disrupt the complex III role, resulting in compromised electron flow and diminished ATP production. Furthering the understanding of ROSI's impact on mitochondrial complexes, an additional marked downregulation in mitochondrially encoded cytochrome c oxidase I (MT-CO1) was observed. The MT-CO1 protein is a pivotal subunit of cytochrome c oxidase, the terminal enzyme in the electron transport chain, serving as an electron acceptor, mediating the transfer of electrons from cytochrome c to oxygen and driving the synthesis of ATP (R. K. Singh et al., 2019). Its downregulation strongly reflects the direct interplay between ROSI and mitochondrial complexes. In parallel with the downregulation in pyruvate metabolism and the citric acid cycle noted in response to TZD treatment, an upregulation in lactate dehydrogenase was observed, suggesting an adaptive response to limited oxygen availability (hypoxic state), allowing cells to compensate for the limited energy

supply. This proposed theory is strongly supported by the upregulation of the hypoxia-inducible factor 1 (HIF-1) pathway identified in the PGZ- and ROSI-KEGG analyses. As such, it seems that TZDs induced mitochondrial damage that led to AC16 cells' death due to a decline in ATP production.

4.1.2 | Molecular insights into TZD-induced AC16 cellular death

The induction of energy deficit, oxidative stress and hypoxia often culminates in cellular death. Regardless of whether cell death is an endpoint or a sign of impending disease progression, it is a common pathological mechanism that underpins all CVDs. However, there are distinct types of cell death, and they are disease-dependent to a substantial extent.

To investigate the type of cell death in AC16 cells treated with TZD agents, the level of apoptosis was examined by measuring caspase 3/7 activity. It was found that this activity was not markedly elevated in the TZD-treated cells apart from the observation endpoints noted in ROSI-treated AC16 cells, suggesting the following: (i) PGZ could have inhibitory effects on caspase-dependent apoptosis, consistent with a previous in vivo study findings conducted on adult male Sprague–Dawley rats (J. Li et al., 2008). (ii) The activation in caspase 3/7 that we noted in ROSI-treated AC16 cells was also noted in another in vitro study, in which ROSI treatment induced apoptosis at 50 and 60 μM in cultured H9c2 cells (Mishra et al., 2014). A possible explanation is that apoptosis activation could be downstream of mitochondrial uncoupling, leading to activation of the caspase cascade (Zorova et al., 2018).

Interestingly, our toxicoproteomics analysis uncovered that two forms of cell death were shared between PGZ and ROSI. One of which includes necroptosis. Compared with apoptosis, necroptosis is a regulated caspase-independent process that correlates at the molecular level with the activation of receptor-interacting protein kinases 1 and 3 (RIPK1 and RIPK3) (Dhuriya & Sharma, 2018; Xue et al., 2020).

With reference to the PGZ dataset, enrichment in the necroptosis pathway, which was characterised primarily by the upregulation of phosphoglycerate mutase family member 5 (PGAM5) and dynamin-related protein 1 (Drp1), strongly suggested that mitochondrial-mediated necroptosis occurred in PGZ-treated AC16 cells. PGAM5 is a mitochondrial phosphatase integral in the regulation of mitochondrial dynamics (i.e. mitochondrial fission) and various types of cell death, including mitophagy and necroptosis (Cheng et al., 2021). In the context of necroptosis, emerging evidence indicates that PGAM5 is the point of convergence for multiple necrosis pathways (Cheng et al., 2021; Z. Wang et al., 2012). Nevertheless, it is defined as a downstream molecule of protein serine/threonine kinase receptor interacting protein 1/ Mixed lineage kinase domain like pseudokinase (RIP3/MLKL), and its RIPK3-dependent activation results in its recruitment to the mitochondria (Cheng et al., 2021; Z. Wang et al., 2012; Xue et al., 2020). Activated PGAM5 subsequently dephosphorylates and activates the mitochondrial fission factor Drp1 and its GTPase activity, leading to mitochondrial fragmentation, an obligatory step in the execution of necroptosis (Cheng et al., 2021; Z. Wang et al., 2012; Xue et al., 2020). Surprisingly, our toxicoproteomics analysis indicated that the enhanced expression of proteins in the PGAM5–Drp1 axis was independent of the canonical necroptosis pathway. This finding has also been reported elsewhere, with PGAM5 reported to play an indispensable role in mediating concanavalin A-induced liver injury without being implicated in the execution of the canonical necroptosis pathway (He et al., 2017). Collectively, these findings may suggest that a novel form of PGAM5–Drp1 axis-mediated necrosis exists, and this necessitates further investigation.

Surprisingly, ROSI counteracts the effect of PGZ on necroptosis. The proteome profile of ROSI-treated cells showed downregulation of glutamate dehydrogenase (GLUD), a protein reported to play a role in the initiation and execution of necroptosis (Morgan & Kim, 2022). An explanation of GLUD enzyme contribution to necroptosis execution is its interaction with RIPK3 and thereby activating necroptosis signalling (Morgan & Kim, 2022). Hence, the dysregulation of GLUD suggests an inhibitory effect of ROSI against necroptosis.

The second pathway that exhibited enrichment in both drugs was ferroptosis. Ferroptosis is defined as an iron-dependent type of non-apoptotic cell death that is primarily characterised by two main biochemical features: iron accumulation and lipid peroxidation (W. Hu et al., 2022). There have been mixed results regarding the effect of TZDs on ferroptosis (Chen et al., 2020; Liang et al., 2022). However, in our analysis, TZDs showed a strong ferroptosis inhibitory effect mediated by glutathione peroxidase-4 (GPX4)-dependent (PGZ only) and independent pathways (PGZ and ROSI). Exposing AC16 cells to PGZ led to significant upregulation of the antioxidant defence enzyme GPX4, a cornerstone regulator of ferroptosis (W. Hu et al., 2022). Because ferroptosis is triggered by iron-dependent lipid peroxidation accumulation, the induction of GPX4 production, which functionally disrupts lipid peroxidation by converting lipid hydroperoxides into nontoxic lipid alcohols, will eventually result in ferroptosis suppression. In addition to this GPX4-dependent inhibitory effect, the expression of ferritin was significantly upregulated in both ROSI- and PGZ-treated cells, suggesting a GPX4-independent mechanism for ferroptosis inhibition. Upregulation of ferritin, the iron-storage form, can limit the availability of iron in the body and thus limit ferroptosis (Ma et al., 2022). Another GPX4-independent pathway revealed by our analysis and implicated only in PGZ-mediated ferroptosis inhibition is the interaction of PGZ with CDGSH iron–sulphur domain-containing protein 1 (mitoNEET), an outer mitochondrial membrane protein that plays a crucial role in mitochondrial iron homeostasis (Kharechkina et al., 2021). MitoNEET is reportedly a mitochondrial PGZ target and has been shown to be overexpressed in various compartments, including the heart (Kharechkina et al., 2021; Yuan et al., 2016). Loss of mitoNEET, as reported by cumulative evidence, leads to intracellular iron accumulation that results in excessive reactive oxygen species (ROS) generation and, therefore, ferroptosis (Yuan et al., 2016). In our analysis, upregulation of the anti-ferroptosis

activity of mitoNEET was noted in the PGZ-treated samples. Together with the abovementioned findings, this result supports the notion that PGZ and ROSI have anti-ferroptosis activity.

4.2 | Deciphering the molecular mechanisms of cardiotoxicity: a drug-specific perspective

4.2.1 | ROSI and alteration in myocyte contractility

The present study has revealed the 'cardiac muscle contraction' pathway as a novel contributor to ROSI-induced cardiotoxicity, representing a significant advancement in our understanding of this adverse drug reaction. The characterisation of the enriched proteins in this tightly regulated pathway points towards four possible explanations by which ROSI modulates cardiomyocyte contraction: (i) impediment in cardiac muscle metabolism primarily through interrupting the oxidative phosphorylation process via altering mitochondrial complexes levels (MT-CO1 and UQCRC1) and (ii) alteration in muscle coordination, as significant downregulation in myosin light chain 3 (MYL3) was noted. This downregulation in MYL3 could drastically reduce myosin phosphorylation, disrupting the myosin–actin interaction and thereby compromising muscle contractility (Sitbon et al., 2020). (iii) Perturbation in catecholamine synthesis is another mechanism suggested herein, following the downregulation in aspartate beta-hydroxylase (ASPH) noted with ROSI-treated cells. The dysregulation in ASPH enzymes involved in catecholamine synthesis could principally lead to a reduction in sympathetic nervous system activity manifested in low heart rate, decreased contractility and impaired blood pressure regulation (Brewitz et al., 2020), and finally, (iv) modulation in cardiac sodium pump (Na^+/K^+ ATPase) function. Our findings revealed significant downregulation of ATPase Na^+/K^+ transporting subunit alpha 1 (ATP1A1), a major component of Na^+/K^+ pump that has a recognisable role in maintaining the electrochemical gradient that arises from the difference in electrical potential and ion concentration across the cell membrane (Obradovic et al., 2023). Hence, dysregulation in ATP1A1 associated with ROSI exposure could have a dramatic effect on the contractile machinery, which could potentially result in elevating cytosolic calcium levels, leading to sustained muscle contraction and, eventually, muscle weakness.

4.2.2 | ROSI influence on protein synthesis machinery

Noticeably reported in association with ROSI, the GO and KEGG observations suggest modulation in the cellular machinery responsible for the protein synthesis reflected by 'ribosome pathway', 'protein export' and 'protein processing in the endoplasmic reticulum (ER)'. The analysis revealed a downregulation of various numbers of ribosomal proteins, including ribosomal protein L24, which play a crucial role in the decoding of mRNA during translation and thus impede protein synthesis (Kisly et al., 2019). Moreover, downregulation of SEC61 translocon subunit alpha 1 (SEC61A1), a pivotal subunit of the transmembrane protein SEC61 that mediates the translocation of the newly synthesised proteins from the cytoplasm to the ER for proper folding and protein maturation (i.e. glycosylation and disulphide bond formation) (Lang et al., 2017), was noted. The effect of ROSI on protein machinery also extends to involving other proteins localised in the endoplasmic recticulum (ER), with crucial roles in protein folding. This includes downregulation in ribophorin 1, a chaperone-like protein that facilitates N-linked glycosylation to the asparagine residues on proteins (Wilson & High, 2007), and protein disulphide isomerase family A member 3, which catalyses the formation and isomerization of disulphide bonds between cysteine residues in proteins (Ali Khan & Mutus, 2014). Altogether, the decreased expression of the abovementioned proteins reveals critical insights into the disruption of protein machinery, protein export and protein processing in the ER that could massively lead to defects in protein maturation, accumulation of unfolded or misfolded proteins in the ER and, ultimately, disruption in ER homeostasis.

4.2.3 | Immunothrombotic dysregulation and cytoskeleton architecture alteration in PGZ-treated AC16 cells

The interplay between the complement and coagulation cascades

HF is well-recognised as a disorder of cardiac contractility. Despite the phenotypic and pathophysiological heterogeneity of contractile failure, alterations in blood coagulation status and cardiomyocyte cytoskeleton components responsible for preserving cell morphology and orchestrating contractile activity play a central part. In the current study, PGZ treatment led to activation of the complement system and coagulation cascade, and this was reflected by enhanced expression of numerous complement proteins, including complement C5, C7 and C9, and various coagulation factors (i.e. coagulation factor II, V and IX). Three potential mechanisms responsible for this upregulation in the complement and coagulation cascades and their interconnectivity are briefly explained below. First, the upregulation noted in the complement components, coagulation factors and scar constituents (i.e. collagens) may suggest that their enhanced expression was part of an adaptive response to PGZ-induced myocardial damage/stress that led to an immune-cell response and scar formation. Clinically, the involvement of the complement system in HF pathogenesis is well-known. For example, Aukrust et al. (2001) reported an increase in complement activation in patients with HF, including those with dilated and ischaemic cardiomyopathies. Second, our data showed that there was a molecular alteration in coagulation proteins and upregulation in the platelet activity pathway, suggesting an increased risk of blood clotting associated with PGZ exposure. Interestingly, these findings are in agreement with those from clinical cases that have reported an increase in blood coagulation with PGZ treatment (Jarrar et al., 2022). Therefore, PGZ's intrinsic ability to increase blood

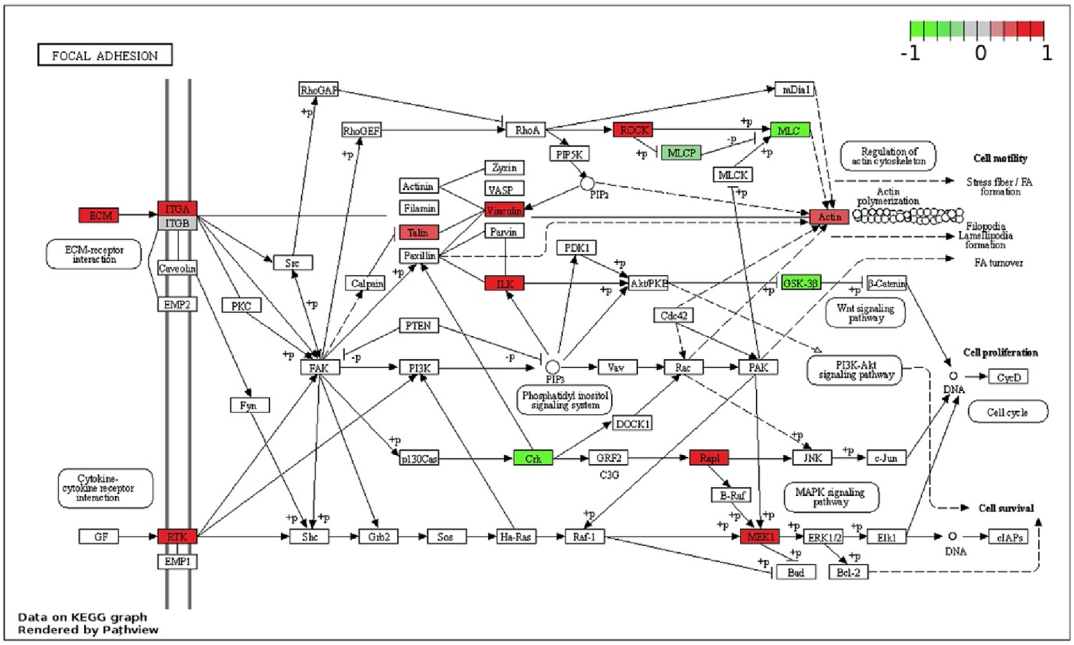

FIGURE 8 The focal adhesion signalling pathway. Proteins expression in the focal adhesion pathway (Kyoto Encyclopedia of Genes and Genomes [KEGG]: 04510) with respect to our measured proteomics data. Red represents up-regulated proteins, while green represents down-regulated proteins. The plot was generated using PATHVIEW (available online: https://pathview.uncc.edu/analysis).

clotting and thrombus formation may result in complement activation by way of thrombus-mediated complement activation, as described in detail by de Bont et al. (2019), and consequently immunoinflammatory reactions. Third, necroptosis induced by PGZ exposure could lead to complement activation. In turn, complement activation can promote fibrin and clot formation.

Perturbation of cell–matrix adhesion in PGZ-treated cells

The cardiac ECM, a highly dynamic non-cellular network, plays a crucial role in cellular development and haemostasis (Frantz et al., 2010). However, aberrant protein expression in the ECM could adversely impact cellular integrity and ultimately contribute to various CVD pathologies, including HF (Frangogiannis, 2019; Frantz et al., 2010). The current study's findings showed that there was an upregulation in the ECM receptor–FA–cytoskeleton pathway axis. The upregulation of ECM proteins was reflected by increased myocardial collagen and fibronectin levels, along with enhanced expression of the integrin receptors, heterodimeric transmembrane proteins consisting of α and β subunits, suggesting that the cell–matrix adhesion/linkages were modulated by PGZ exposure.

Changes in the ECM profile can be sensed by cells via active mechanosensing, a process primarily mediated by integrins (P. Hu et al., 2023; Huveneers & Danen, 2009). When integrins bind their adhesive ligands, a conformational change occurs in the integrin's cytoplasmic domain, and this triggers the formation of docking sites, allowing the recruitment of anchor and cytoskeleton proteins, such as talin and vinculin, which are responsible for initiating signalling cascades and links to the cytoskeleton (P. Hu et al., 2023; Huveneers & Danen, 2009). These proteins were overexpressed in PGZ-treated cells. The resultant integrin–anchor protein complexes ultimately support integrin clustering and the formation of FAs between a cell and the ECM (P. Hu et al., 2023; Huveneers & Danen, 2009). The formation of FAs results in the activation and recruitment of other adapter proteins, including integrin-linked kinase (Yen et al., 2014), which was overexpressed in the treated cells in this study. This subsequently causes the activation of various downstream signalling pathways implicated in regulating cell behaviour and cytoskeleton organisation (Yen et al., 2014).

It is likely that PGZ affects the cytoskeleton of cardiomyocytes by targeting the talin–vinculin axis and the Rho-associated kinases (ROCK1 and ROCK2) pathway (Figure 8). The crosslinking of vinculin with talin and actin is fundamental in the orchestration of the actomyosin cytoskeleton's actions (Meagher et al., 2021). Aberrant expression in the talin–vinculin axis could result in detrimental effects on actin polymerisation and, ultimately, myocardial stiffness. Our findings align with those from an RNA-sequencing analysis performed to investigate changes in cytoskeletal genes in patients with ischaemic and dilated cardiomyopathy (Herrer et al., 2014). In that analysis, increased vinculin expression was noted and reported to be associated with HF pathogenesis (Herrer et al., 2014; Meagher et al., 2021; Yen et al., 2014). Furthermore, in another study, knocking out mouse cardiomyocyte talin-1 resulted in a reduction in cardiac hypertrophy and fibrosis compared with that in wild-type mice (Manso et al., 2017).

Integrin activation following PGZ exposure has also been shown to upregulate the Rho/ROCK pathway. When Rho is activated via

integrins, it activates ROCK1 and ROCK2, and this leads to the phosphorylation of several downstream substrates, including myosin phosphatase target subunit 1, ezrin–radixin–moesin and myosin light chain (MLC), which is crucial for diverse cellular responses (Hartmann et al., 2015). Nevertheless, the high expression of ROCK1 and ROCK2 found in our analysis was concomitant with the downregulation of MLC and MLC kinase, which may be an attempt to compensate for the increased Rho kinase activity, as explained by Kirschstein et al. (2015). This downregulation of MLC may ultimately result in a decrease in myocardial flexibility and increased myocardial stiffness, as proven by numerous studies (Hartmann et al., 2015; Herrer et al., 2014; Manso et al., 2017).

4.3 | Limitations and future directions

Although the study provides valuable insights, it is crucial to acknowledge that it has a few limitations that should be considered before drawing a definitive conclusion. In response to the NRC's call, the adoption of in vitro-*to*-in vivo extrapolation methodologies over animal experimentation is becoming increasingly popular in mechanistic toxicology studies. Motivated by this rationale, a cell model represented by AC16 cells was employed in this study. The AC16 cell line is derived from adult human ventricular cardiomyocytes (Davidson et al., 2005). This affordable, immortalised, stable cell line has been used widely in toxicology research, as the cells express adult cardiomyocyte-specific biomarkers (α-myosin heavy chain [α-MHC], β-MHC, α-actin and troponin I) and display electrophysiological properties that are comparable to those of primary human cardiomyocytes (Davidson et al., 2005). While cell models offer numerous advantages, they have some limitations. In vitro models, despite their contributions, cannot accurately reflect the biological complexity of the human body. Also, when investigating the proteomic activity of cells, using an in vitro model could be a limitation because such models exhibit restricted proteomic activity compared with in vivo systems.

In conclusion, we have conducted a comprehensive study comprised of a novel toxicoproteomics pipeline and a cytotoxicity analysis to elucidate the effects of TZDs on the cardiac cell. The findings provide substantial mechanistic insight into the role mitochondrial dysfunction plays in TZDs' undesirable actions. Furthermore, our investigation sheds light on novel mechanisms, pathways and proteins that could mediate the detrimental effects that TZD has on cardiomyocytes. These findings therefore present promising targets for developing strategies to mitigate these undesirable effects and improve TZD safety profiles. Nevertheless, further functional and clinical investigations are necessary to validate the roles these potential targets play in TZD cytotoxicity.

CONFLICT OF INTEREST STATEMENT

The authors have no conflict of interest to report.

DATA AVAILABILITY STATEMENT

The data that support the findings of this study are openly available in Pride Database at https://www.ebi.ac.uk/pride/markdownpage/submitdatapage, reference number PXD048231.

ORCID

Zahra Rattray https://orcid.org/0000-0002-8371-8549

Nicholas J. W. Rattray https://orcid.org/0000-0002-3528-6905

REFERENCES

Ahn, J. H., Seo, H., Park, W., Seok, J., Lee, J. A., Kim, W. J., Kim, G. B., Kim, K. J., & Lee, S. Y. (2020). Enhanced succinic acid production by Mannheimia employing optimal malate dehydrogenase. *Nature Communications*, *11*(1), 1970. https://doi.org/10.1038/s41467-020-15839-z

Al Sultan, A., Rattray, Z., & Rattray, N. J. (2023). Cytotoxicity and toxicoproteomic analysis of pioglitazone exposure in human-derived cardiomyocytes.

Al Sultan, A., Rattray, Z., & Rattray, N. J. (2024). Toxicometabolomics-based cardiotoxicity evaluation of thiazolidinedione exposure in human-derived cardiomyocytes. *Metabolomics*, *20*(2), 24. https://doi.org/10.1007/s11306-024-02097-z

Ali Khan, H., & Mutus, B. (2014). Protein disulfide isomerase a multifunctional protein with multiple physiological roles. *Frontiers in Chemistry*, *2*, 70.

Association, A. D. (2023). Standards of care in diabetes—2023 abridged for primary care providers. *Clinical Diabetes*, *41*(1), 4–31. https://doi.org/10.2337/cd23-as01

Aukrust, P., Gullestad, L., Lappegård, K. T., Ueland, T., Aass, H., Wikeby, L., Simonsen, S., Frøland, S. S., & Mollnes, T. E. (2001). Complement activation in patients with congestive heart failure: Effect of high-dose intravenous immunoglobulin treatment. *Circulation*, *104*(13), 1494–1500. https://doi.org/10.1161/hc3801.096353

Brewitz, L., Tumber, A., Pfeffer, I., McDonough, M. A., & Schofield, C. J. (2020). Aspartate/asparagine-β-hydroxylase: A high-throughput mass spectrometric assay for discovery of small molecule inhibitors. *Scientific Reports*, *10*(1), 8650. https://doi.org/10.1038/s41598-020-65123-9

Busiello, R. A., Savarese, S., & Lombardi, A. (2015). Mitochondrial uncoupling proteins and energy metabolism. *Frontiers in Physiology*, *6*, 36. https://doi.org/10.3389/fphys.2015.00036

Chen, X., Yu, C., Kang, R., & Tang, D. (2020). Iron metabolism in ferroptosis. *Frontiers in Cell and Developmental Biology*, *8*, 590226. https://doi.org/10.3389/fcell.2020.590226

Cheng, M., Lin, N., Dong, D., Ma, J., Su, J., & Sun, L. (2021). PGAM5: A crucial role in mitochondrial dynamics and programmed cell death. *European Journal of Cell Biology*, *100*(1), 151144. https://doi.org/10.1016/j.ejcb.2020.151144

Davidson, M., Nesti, C., Palenzuela, L., Walker, W., Hernandez, E., Protas, L., Hirano, M., & Isaac, N. (2005). Novel cell lines derived from adult human ventricular cardiomyocytes. *Journal of Molecular and Cellular Cardiology*, *39*(1), 133–147. https://doi.org/10.1016/j.yjmcc.2005.03.003

de Bont, C. M., Boelens, W. C., & Pruijn, G. J. (2019). NETosis, complement, and coagulation: A triangular relationship. *Cellular & Molecular Immunology*, *16*(1), 19–27. https://doi.org/10.1038/s41423-018-0024-0

De Flines, J., & Scheen, A. J. (2007). Glitazones and congestive heart failure: Update on PROactive, ADOPT, DREAM and RECORD clinical trials. *Revue Médicale Suisse*, *3*(122) 1876, 1878–1883, 1878–1883.

de Jong, M., van der Worp, H. B., van der Graaf, Y., Visseren, F. L., & Westerink, J. (2017). Pioglitazone and the secondary prevention of cardiovascular disease. A meta-analysis of randomized-controlled trials. *Cardiovascular Diabetology*, *16*(1), 1–11.

DeFronzo, R. A., Mehta, R. J., & Schnure, J. J. (2013). Pleiotropic effects of thiazolidinediones: Implications for the treatment of patients with type 2 diabetes mellitus. *Hospital Practice*, *41*(2), 132–147. https://doi.org/10.3810/hp.2013.04.1062

Demine, S., Renard, P., & Arnould, T. (2019). Mitochondrial uncoupling: A key controller of biological processes in physiology and diseases. *Cells*, *8*(8), 795. https://doi.org/10.3390/cells8080795

Dhuriya, Y. K., & Sharma, D. (2018). Necroptosis: A regulated inflammatory mode of cell death. *Journal of Neuroinflammation*, *15*(1), 199. https://doi.org/10.1186/s12974-018-1235-0

Frangogiannis, N. G. (2019). The extracellular matrix in ischemic and nonischemic heart failure. *Circulation Research*, *125*(1), 117–146. https://doi.org/10.1161/CIRCRESAHA.119.311148

Frantz, C., Stewart, K. M., & Weaver, V. M. (2010). The extracellular matrix at a glance. *Journal of Cell Science*, *123*(24), 4195–4200. https://doi.org/10.1242/jcs.023820

Ghasemi, M., Liang, S., Luu, Q. M., & Kempson, I. (2023). The MTT assay: A method for error minimization and interpretation in measuring cytotoxicity and estimating cell viability. In *Cell viability assays: Methods and protocols* (pp. 15–33). Springer. https://doi.org/10.1007/978-1-0716-3052-5_2

Goutelle, S., Maurin, M., Rougier, F., Barbaut, X., Bourguignon, L., Ducher, M., & Maire, P. (2008). The Hill equation: A review of its capabilities in pharmacological modelling. *Fundamental & Clinical Pharmacology*, *22*(6), 633–648. https://doi.org/10.1111/j.1472-8206.2008.00633.x

Hartmann, S., Ridley, A. J., & Lutz, S. (2015). The function of Rho-associated kinases ROCK1 and ROCK2 in the pathogenesis of cardiovascular disease. *Frontiers in Pharmacology*, *6*, 276. https://doi.org/10.3389/fphar.2015.00276

He, G.-W., Günther, C., Kremer, A. E., Thonn, V., Amann, K., Poremba, C., Neurath, M. F., Wirtz, S., & Becker, C. (2017). PGAM5-mediated programmed necrosis of hepatocytes drives acute liver injury. *Gut*, *66*(4), 716–723. https://doi.org/10.1136/gutjnl-2015-311247

Herrer, I., Roselló-Lletí, E., Rivera, M., Molina-Navarro, M. M., Tarazón, E., Ortega, A., Martínez-Dolz, L., Triviño, J. C., Lago, F., González-Juanatey, J. R., Bertomeu, V., Montero, J. A., & Portolés, M. (2014). RNA-sequencing analysis reveals new alterations in cardiomyocyte cytoskeletal genes in patients with heart failure. *Laboratory Investigation*, *94*(6), 645–653. https://doi.org/10.1038/labinvest.2014.54

Hu, P., Miller, A. E., Yeh, C.-R., Bingham, G. C., Civelek, M., & Barker, T. H. (2023). SEMA7a primes integrin α5β1 engagement instructing fibroblast mechanotransduction, phenotype and transcriptional programming. *Matrix Biology*, *121*, 179–193. https://doi.org/10.1016/j.matbio.2023.06.006

Hu, W., Liang, K., Zhu, H., Zhao, C., Hu, H., & Yin, S. (2022). Ferroptosis and its role in chronic diseases. *Cells*, *11*(13), 2040. https://doi.org/10.3390/cells11132040

Huveneers, S., & Danen, E. H. (2009). Adhesion signaling–crosstalk between integrins, Src and Rho. *Journal of Cell Science*, *122*(8), 1059–1069. https://doi.org/10.1242/jcs.039446

Jarrar, Y. B., Jarrar, Q., Abaalkhail, S. J., Moh'd Kalloush, H., Naser, W., Zihlif, M., al Shhab, M., el Madani, A., Jamous, Y., & Lee, S. J. (2022). Molecular toxicological alterations in the mouse hearts induced by sub-chronic thiazolidinedione drugs administration. *Fundamental & Clinical Pharmacology*, *36*(1), 143–149. https://doi.org/10.1111/fcp.12694

Joon, H. K., Thalor, A., & Gupta, D. (2023). Machine learning analysis of lung squamous cell carcinoma gene expression datasets reveals novel prognostic signatures. *Computers in Biology and Medicine*, *165*, 107430. https://doi.org/10.1016/j.compbiomed.2023.107430

Kharechkina, E. S., Nikiforova, A. B., Belosludtsev, K. N., Rokitskaya, T. I., Antonenko, Y. N., & Kruglov, A. G. (2021). Pioglitazone is a mild carrier-dependent uncoupler of oxidative phosphorylation and a modulator of mitochondrial permeability transition. *Pharmaceuticals*, *14*(10), 1045. https://doi.org/10.3390/ph14101045

Kirschstein, T., Sahre, T., Kernig, K., Protzel, C., Porath, K., Köhling, R., & Hakenberg, O. W. (2015). Inverse relationship of Rho kinase and myosin-light chain kinase expression in the aging human detrusor smooth muscle. *BMC Urology*, *15*(1), 104. https://doi.org/10.1186/s12894-015-0098-2

Kisly, I., Remme, J., & Tamm, T. (2019). Ribosomal protein eL24, involved in two intersubunit bridges, stimulates translation initiation and elongation. *Nucleic Acids Research*, *47*(1), 406–420. https://doi.org/10.1093/nar/gky1083

Kolde, R., & Kolde, M. R. (2015). Package 'pheatmap'. *R package*, *1*(7), 790.

Krijthe, J., van der Maaten, L., & Krijthe, M. J. (2018). Package 'Rtsne'. R package version 0.13.

Lago, R. M., Singh, P. P., & Nesto, R. W. (2007). Congestive heart failure and cardiovascular death in patients with prediabetes and type 2 diabetes given thiazolidinediones: A meta-analysis of randomised clinical trials. *The Lancet*, *370*(9593), 1129–1136. https://doi.org/10.1016/S0140-6736(07)61514-1

Lang, S., Pfeffer, S., Lee, P.-H., Cavalié, A., Helms, V., Förster, F., & Zimmermann, R. (2017). An update on Sec61 channel functions, mechanisms, and related diseases. *Frontiers in Physiology*, *8*, 887. https://doi.org/10.3389/fphys.2017.00887

Langfelder, P., & Horvath, S. (2008). WGCNA: An R package for weighted correlation network analysis. *BMC Bioinformatics*, *9*(1), 559. https://doi.org/10.1186/1471-2105-9-559

Li, J., Lang, M.-J., Mao, X.-B., Tian, L., & Feng, Y.-B. (2008). Antiapoptosis and mitochondrial effect of pioglitazone preconditioning in the ischemic/reperfused heart of rat. *Cardiovascular Drugs and Therapy*, *22*, 283–291. https://doi.org/10.1007/s10557-008-6115-x

Li, Y., Ma, L., Wu, D., & Chen, G. (2021). Advances in bulk and single-cell multi-omics approaches for systems biology and precision medicine. *Briefings in Bioinformatics*, *22*(5), bbab024. https://doi.org/10.1093/bib/bbab024

Liang, H., Tang, T., Huang, H., Li, T., Gao, C., Han, Y., Yuan, B., Gao, S., Wang, H., & Zhou, M. L. (2022). Peroxisome proliferator-activated receptor-γ ameliorates neuronal ferroptosis after traumatic brain injury in mice by inhibiting cyclooxygenase-2. *Experimental Neurology*, *354*, 114100. https://doi.org/10.1016/j.expneurol.2022.114100

Liao, H.-W., Saver, J. L., Wu, Y.-L., Chen, T.-H., Lee, M., & Ovbiagele, B. (2017). Pioglitazone and cardiovascular outcomes in patients with insulin resistance, pre-diabetes and type 2 diabetes: A systematic review and meta-analysis. *BMJ Open*, *7*(1), e013927. https://doi.org/10.1136/bmjopen-2016-013927

Liu, S., Zeng, F., Fan, G., & Dong, Q. (2021). Identification of hub genes and construction of a transcriptional regulatory network associated with tumor recurrence in colorectal cancer by weighted gene co-expression network analysis. *Frontiers in Genetics*, *12*, 649752. https://doi.org/10.3389/fgene.2021.649752

Ma, T., Du, J., Zhang, Y., Wang, Y., Wang, B., & Zhang, T. (2022). GPX4-independent ferroptosis—A new strategy in disease's therapy. *Cell Death Discovery*, *8*(1), 434. https://doi.org/10.1038/s41420-022-01212-0

Manso, A. M., Okada, H., Sakamoto, F. M., Moreno, E., Monkley, S. J., Li, R., Critchley, D. R., & Ross, R. S. (2017). Loss of mouse cardiomyocyte talin-1 and talin-2 leads to β-1 integrin reduction, costameric instability, and dilated cardiomyopathy. *Proceedings of the National Academy of Sciences*, *114*(30), E6250–E6259. https://doi.org/10.1073/pnas.1701416114

Meagher, P. B., Lee, X. A., Lee, J., Visram, A., Friedberg, M. K., & Connelly, K. A. (2021). Cardiac fibrosis: Key role of integrins in cardiac

homeostasis and remodeling. *Cells*, *10*(4), 770. https://doi.org/10.3390/cells10040770

Mishra, P., Singh, S. V., Verma, A. K., Srivastava, P., Sultana, S., & Rath, S. K. (2014). Rosiglitazone induces cardiotoxicity by accelerated apoptosis. *Cardiovascular Toxicology*, *14*, 99–119. https://doi.org/10.1007/s12012-013-9234-y

Morgan, M. J., & Kim, Y.-S. (2022). Roles of RIPK3 in necroptosis, cell signaling, and disease. *Experimental & Molecular Medicine*, *54*(10), 1695–1704. https://doi.org/10.1038/s12276-022-00868-z

Nguyen, N., Jennen, D., & Kleinjans, J. (2022). Omics technologies to understand drug toxicity mechanisms. *Drug Discovery Today*, *27*, 103348. https://doi.org/10.1016/j.drudis.2022.103348

Niles, A. L., Moravec, R. A., & Riss, T. L. (2008). Caspase activity assays. In *Apoptosis and cancer Methods and protocols* (pp. 137–150). https://doi.org/10.1007/978-1-59745-339-4_11

Nissen, S. E., & Wolski, K. (2007). Effect of rosiglitazone on the risk of myocardial infarction and death from cardiovascular causes. *New England Journal of Medicine*, *356*(24), 2457–2471. https://doi.org/10.1056/NEJMoa072761

Nissen, S. E., & Wolski, K. (2010). Rosiglitazone revisited: An updated meta-analysis of risk for myocardial infarction and cardiovascular mortality. *Archives of Internal Medicine*, *170*(14), 1191–1201. https://doi.org/10.1001/archinternmed.2010.207

Nury, C., Merg, C., Eb-Levadoux, Y., Bovard, D., Porchet, M., Maranzano, F., Loncarevic, I., Tavalaei, S., Lize, E., Demenescu, R. L., Yepiskoposyan, H., Hoeng, J., Ivanov, N. V., Renggli, K., & Titz, B. (2023). Toxicoproteomics reveals an effect of clozapine on autophagy in human liver spheroids. *Toxicology Mechanisms and Methods*, *33*(5), 401–410. https://doi.org/10.1080/15376516.2022.2156005

Obradovic, M., Sudar-Milovanovic, E., Gluvic, Z., Banjac, K., Rizzo, M., & Isenovic, E. R. (2023). The Na+/K+-ATPase: A potential therapeutic target in cardiometabolic diseases. *Frontiers in Endocrinology*, *14*, 1150171. https://doi.org/10.3389/fendo.2023.1150171

Richter, B., Bandeira-Echtler, E., Bergerhoff, K., Clar, C., & Ebrahim, S. H. (2007). Rosiglitazone for type 2 diabetes mellitus. *Cochrane Database of Systematic Reviews*, *3*. https://doi.org/10.1002/14651858.CD006063.pub2

Singh, R. K., Saini, S. K., Prakasam, G., Kalairasan, P., & Bamezai, R. N. (2019). Role of ectopically expressed mtDNA encoded cytochrome c oxidase subunit I (MT-COI) in tumorigenesis. *Mitochondrion*, *49*, 56–65. https://doi.org/10.1016/j.mito.2019.07.002

Singh, S., Loke, Y. K., & Furberg, C. D. (2007a). Long-term risk of cardiovascular events with rosiglitazone: A meta-analysis. *Jama*, *298*(10), 1189–1195. https://doi.org/10.1001/jama.298.10.1189

Singh, S., Loke, Y. K., & Furberg, C. D. (2007b). Thiazolidinediones and heart failure: A teleo-analysis. *Diabetes Care*, *30*(8), 2148–2153. https://doi.org/10.2337/dc07-0141

Sitbon, Y. H., Yadav, S., Kazmierczak, K., & Szczesna-Cordary, D. (2020). Insights into myosin regulatory and essential light chains: A focus on their roles in cardiac and skeletal muscle function, development and disease. *Journal of Muscle Research and Cell Motility*, *41*, 313–327. https://doi.org/10.1007/s10974-019-09517-x

Starner, C. I., Schafer, J. A., Heaton, A. H., & Gleason, P. P. (2008). Rosiglitazone and pioglitazone utilization from January 2007 through May 2008 associated with five risk-warning events. *Journal of Managed Care Pharmacy*, *14*(6), 523–531. https://doi.org/10.18553/jmcp.2008.14.6.523

Tan, Y., Wang, M., Yang, K., Chi, T., Liao, Z., & Wei, P. (2021). PPAR-α modulators as current and potential cancer treatments. *Frontiers in Oncology*, *11*, 599995. https://doi.org/10.3389/fonc.2021.599995

Thomas, S., Ricke, W. A., & Li, L. (2023). Toxicoproteomics of mono (2-ethylhexyl) phthalate and perfluorooctanesulfonic acid in models of prostatic diseases. *Chemical Research in Toxicology*, *36*(2), 251–259. https://doi.org/10.1021/acs.chemrestox.2c00328

Valcarcel-Jimenez, L., & Frezza, C. (2023). Fumarate hydratase (FH) and cancer: A paradigm of oncometabolism. *British Journal of Cancer*, *129*(10), 1546–1557. https://doi.org/10.1038/s41416-023-02412-w

Vuda, M., & Kamath, A. (2016). Drug induced mitochondrial dysfunction: Mechanisms and adverse clinical consequences. *Mitochondrion*, *31*, 63–74. https://doi.org/10.1016/j.mito.2016.10.005

Wajid, S., Menaka, M., Ahmed, F., & Samreen, S. (2019). A literature review on oral hypoglycemic drugs–mechanistic aspects. *Asian Journal of Pharmaceutical and Clinical Research*, *12*(11), 5–10. https://doi.org/10.22159/ajpcr.2019.v12i11.35469

Wallach, J. D., Wang, K., Zhang, A. D., Cheng, D., Grossetta Nardini, H. K., Lin, H., Bracken, M. B., Desai, M., Krumholz, H. M., & Ross, J. S. (2020). Updating insights into rosiglitazone and cardiovascular risk through shared data: Individual patient and summary level meta-analyses. *BMJ*, *368*, l7078. https://doi.org/10.1136/bmj.l7078

Wang, S., Li, W., Hu, L., Cheng, J., Yang, H., & Liu, Y. (2020). NAguideR: Performing and prioritizing missing value imputations for consistent bottom-up proteomic analyses. *Nucleic Acids Research*, *48*(14), e83. https://doi.org/10.1093/nar/gkaa498

Wang, Z., Jiang, H., Chen, S., Du, F., & Wang, X. (2012). The mitochondrial phosphatase PGAM5 functions at the convergence point of multiple necrotic death pathways. *Cell*, *148*(1), 228–243. https://doi.org/10.1016/j.cell.2011.11.030

Wickham, H., Chang, W., & Wickham, M. H. (2016). Package 'ggplot2'. *Create Elegant Data Visualisations Using the Grammar of Graphics Version*, *2*(1), 1–189.

Willforss, J., Chawade, A., & Levander, F. (2018). NormalyzerDE: Online tool for improved normalization of omics expression data and high-sensitivity differential expression analysis. *Journal of Proteome Research*, *18*(2), 732–740. https://doi.org/10.1021/acs.jproteome.8b00523

Wilson, C. M., & High, S. (2007). Ribophorin I acts as a substrate-specific facilitator of N-glycosylation. *Journal of Cell Science*, *120*(4), 648–657. https://doi.org/10.1242/jcs.000729

Wu, J. X., Pascovici, D., Wu, Y., Walker, A. K., & Mirzaei, M. (2021). Application of WGCNA and PloGO2 in the analysis of complex proteomic data. In *Statistical analysis of proteomic data: Methods and tools* (pp. 375–390). Springer.

Xue, C., Gu, X., Li, G., Bao, Z., & Li, L. (2020). Mitochondrial mechanisms of necroptosis in liver diseases. *International Journal of Molecular Sciences*, *22*(1), 66. https://doi.org/10.3390/ijms22010066

Yen, C.-F., Wang, H.-S., Lee, C.-L., & Liao, S.-K. (2014). Roles of integrin-linked kinase in cell signaling and its perspectives as a therapeutic target. *Gynecology and Minimally Invasive Therapy*, *3*(3), 67–72. https://doi.org/10.1016/j.gmit.2014.06.002

Yi, T., Wu, X., & Li, H. (2020). Ubiquinol-cytochrome c reductase core protein 1 overexpression protects H9c2 cardiac cells against mimic ischemia/reperfusion injury through PI3K/Akt/GSK-3β pathway. *Biochemical and Biophysical Research Communications*, *529*(4), 904–909. https://doi.org/10.1016/j.bbrc.2020.06.089

Yu, G., Wang, L.-G., Han, Y., & He, Q.-Y. (2012). clusterProfiler: An R package for comparing biological themes among gene clusters. *OMICS: a Journal of Integrative Biology*, *16*(5), 284–287. https://doi.org/10.1089/omi.2011.0118

Yuan, H., Li, X., Zhang, X., Kang, R., & Tang, D. (2016). CISD1 inhibits ferroptosis by protection against mitochondrial lipid peroxidation. *Biochemical and Biophysical Research Communications*, *478*(2), 838–844. https://doi.org/10.1016/j.bbrc.2016.08.034

Zhang, Q., Ma, C., Gearing, M., Wang, P. G., Chin, L.-S., & Li, L. (2018). Integrated proteomics and network analysis identifies protein hubs and network alterations in Alzheimer's disease. *Acta Neuropathologica Communications*, *6*, 19. https://doi.org/10.1186/s40478-018-0524-2

Zhong, W., Jin, W., Xu, S., Wu, Y., Luo, S., Liang, M., & Chen, L. (2018). Pioglitazone induces cardiomyocyte apoptosis and inhibits cardiomyocyte

hypertrophy via VEGFR-2 signaling pathway. *Arquivos Brasileiros de Cardiologia*, *111*, 162–169. https://doi.org/10.5935/abc.20180108

Zhou, Y., Huang, Y., Ji, X., Wang, X., Shen, L., & Wang, Y. (2020). Pioglitazone for the primary and secondary prevention of cardiovascular and renal outcomes in patients with or at high risk of type 2 diabetes mellitus: A meta-analysis. *The Journal of Clinical Endocrinology & Metabolism*, *105*(5), 1670–1681. https://doi.org/10.1210/clinem/dgz252

Zorova, L. D., Popkov, V. A., Plotnikov, E. Y., Silachev, D. N., Pevzner, I. B., Jankauskas, S. S., Babenko, V. A., Zorov, S. D., Balakireva, A. V., Juhaszova, M., Sollott, S. J., & Zorov, D. B. (2018). Mitochondrial membrane potential. *Analytical Biochemistry*, *552*, 50–59. https://doi.org/10.1016/j.ab.2017.07.009

SUPPORTING INFORMATION

Additional supporting information can be found online in the Supporting Information section at the end of this article.

How to cite this article: Al Sultan, A., Rattray, Z., & Rattray, N. J. W. (2024). Cytotoxicity and toxicoproteomics analysis of thiazolidinedione exposure in human-derived cardiomyocytes. *Journal of Applied Toxicology*, 1–22. https://doi.org/10.1002/jat.4613